



Source sector and region contributions to BC and PM_{2.5} in Central Asia

S. Kulkarni^{1,*}, N. Sobhani^{1,2}, J. P. Miller-Schulze^{3,4}, M. M. Shafer^{3,4}, J. J. Schauer^{3,4}, P. A. Solomon⁵, P. E. Saide¹, S. N. Spak^{1,6}, Y. F. Cheng^{1,**}, H. A. C. Denier van der Gon⁷, Z. Lu⁶, D. G. Streets⁸, G. Janssens-Maenhout⁹, C. Wiedinmyer¹⁰, J. Lantz¹¹, M. Artamonova¹², B. Chen¹³, S. Imashev¹³, L. Sverdlik¹³, J. T. Deminter³, B. Adhikary^{1,***}, A. D'Allura¹⁴, C. Wei^{1,****}, and G. R. Carmichael^{1,2}

¹Center for Global and Regional Environmental Research, University of Iowa, Iowa City, IA, USA

²Department of Chemical & Biochemical Engineering, University of Iowa, Iowa City, IA 52242, USA

³Wisconsin State Laboratory of Hygiene, 2601 Agriculture Drive, Madison, WI 53718, USA

⁴Environmental Chemistry and Technology Program, 660 North Park St, University of Wisconsin, Madison, WI 53706, USA

⁵US EPA, Office of Research & Development, Las Vegas, NV 89193, USA

⁶Public Policy Center, University of Iowa, 223 South Quadrangle, Iowa City, IA 52242, USA

⁷TNO, Princetonlaan 6, 3584 CB Utrecht, the Netherlands

⁸Decision and Information Sciences Division, Argonne National Laboratory, Argonne, IL, USA

⁹European Commission, Joint Research Centre, IES, 21027 Ispra, Italy

¹⁰National Center for Atmospheric Research, Boulder, CO, USA

¹¹US EPA, Office of Radiation and Indoor Air, Las Vegas, NV 89193, USA

¹²Institute of Atmospheric Physics, 109017 Moscow, Russia

¹³Kyrgyz-Russian Slavic University, 44 Kievskaya Str., Bishkek 720000, Kyrgyzstan

¹⁴ARIANET, via Gilino 9, 20128 Milan, Italy

* now at: California Air Resources Board, Sacramento, CA, USA

** now at: Multiphase Chemistry Department, Max Planck Institute for Chemistry, 55128 Mainz, Germany

*** now at: International Centre for Integrated Mountain Development (ICIMOD), GPO Box 3226, Kathmandu, Nepal

**** now at: US EPA, Atmospheric Modeling and Analysis Division, Research Triangle Park, NC, USA

Correspondence to: N. Sobhani (negin-sobhani@uiowa.edu) and G. R. Carmichael (gcarmich@engineering.uiowa.edu)

Received: 24 January 2014 – Published in Atmos. Chem. Phys. Discuss.: 7 May 2014

Revised: 15 December 2014 – Accepted: 27 December 2014 – Published: 18 February 2015

Abstract. Particulate matter (PM) mass concentrations, seasonal cycles, source sector, and source region contributions in Central Asia (CA) are analyzed for the period April 2008–July 2009 using the Sulfur Transport and dEposition Model (STEM) chemical transport model and modeled meteorology from the Weather Research and Forecasting (WRF) model. Predicted aerosol optical depth (AOD) values (annual mean value ~ 0.2) in CA vary seasonally, with lowest values in the winter. Surface PM_{2.5} concentrations (annual mean value

$\sim 10 \mu\text{g m}^{-3}$) also exhibit a seasonal cycle, with peak values and largest variability in the spring/summer, and lowest values and variability in the winter (hourly values from 2 to $90 \mu\text{g m}^{-3}$). Surface concentrations of black carbon (BC) (mean value $\sim 0.1 \mu\text{g m}^{-3}$) show peak values in the winter. The simulated values are compared to surface measurements of AOD as well as PM_{2.5}, PM₁₀, BC, and organic carbon (OC) mass concentrations at two regional sites in Kyrgyzstan (Lidar Station Teplokluchenka (LST) and Bishkek). The pre-

dicted values of AOD and PM mass concentrations and their seasonal cycles are fairly well captured. The carbonaceous aerosols are underpredicted in winter, and analysis suggests that the winter heating emissions are underestimated in the current inventory.

Dust, from sources within and outside CA, is a significant component of the PM mass and drives the seasonal cycles of PM and AOD. On an annual basis, the power and industrial sectors are found to be the most important contributors to the anthropogenic portion of PM_{2.5}. Residential combustion and transportation are shown to be the most important sectors for BC. Biomass burning within and outside the region also contributes to elevated PM and BC concentrations. The analysis of the transport pathways and the variations in particulate matter mass and composition in CA demonstrates that this region is strategically located to characterize regional and intercontinental transport of pollutants. Aerosols at these sites are shown to reflect dust, biomass burning, and anthropogenic sources from Europe; South, East, and Central Asia; and Russia depending on the time period.

Simulations for a reference 2030 emission scenario based on pollution abatement measures already committed to in current legislation show that PM_{2.5} and BC concentrations in the region increase, with BC growing more than PM_{2.5} on a relative basis. This suggests that both the health impacts and the climate warming associated with these particles may increase over the next decades unless additional control measures are taken. The importance of observations in CA to help characterize the changes that are rapidly taking place in the region are discussed.

1 Introduction

Central Asia (CA), a region of republics located between Europe and Asia, faces severe environmental problems, with origins dating back to the 1960s and best symbolized by the Aral Sea catastrophe (Whish-Wilson, 2002). The Aral Sea has shrunk to only about 30 % of its 1960 volume and roughly half its geographical size due to diversion of water for crop cultivation and other purposes. The resulting desertification of the lake bed has resulted in extensive dust storms from the region, which have impacted the surrounding agriculture, ecosystem, and the population's health.

The 2012 Environmental Performance Index (EPI), which tracks performance of 132 countries across a variety of environmental and ecosystem vitality indicators, ranked CA countries among the weakest performers (Kazakhstan: 129; Uzbekistan: 130; Turkmenistan: 131; Tajikistan: 121; and Kyrgyzstan: 101) (Emerson et al., 2012). CA and the surrounding areas are developing quickly and air pollution emissions are projected to increase significantly for the next several decades (Shindell et al., 2012). In recognition of the need to improve the environmental conditions in the region, five

CA countries have formulated the Framework Convention on Preservation of Environment for Sustainable Development of CA (UNEP, 2006).

Despite the awareness of the environmental conditions, it remains an understudied region and there is a general lack of air pollution observations within CA. Furthermore the recent assessment of the intercontinental transport of pollution (HTAP, 2010) has indicated that the major transport pathway of pollution from Europe to Asia is via low-altitude flows passing through CA. The magnitude of the pollution transport from Europe to Asia is highly uncertain, in large part due to the lack of observations of pollutants along this pathway. To help better characterize the air pollution levels and the transport pathways in the region a study was undertaken between scientists from Russia, Kyrgyzstan, and the USA to observe and model aerosols in the region. Measurements of particulate matter (PM) mass and composition were taken at two locations in Kyrgyzstan (Lidar Station Teplokluchenka (LST) and Bishkek) and modeling analysis was performed to assess the contributions of local, regional, and distant sources to the PM concentrations in the region (Miller-Schulze et al., 2012; Chen et al., 2012, 2013).

In this paper we present a modeling analysis of PM_{2.5}, PM₁₀ (PM_{2.5} refers to particles in the size range of less than 2.5 μm aerodynamic diameter (AD) and PM₁₀ refers to particles in the size range of less than 10 μm AD), black carbon (BC), and organic carbon (OC) mass concentrations, and aerosol optical depth (AOD) over the time period of April 2008 to July 2009. The Sulfur Transport and Deposition Model (STEM), a hemispheric chemical transport model (D'Allura et al., 2011), is used to estimate spatial and temporal variations in PM in CA, and to assess the contributions to PM from wind-blown dust, open biomass burning, and anthropogenic sources, as well as different geographical source regions and source sectors (transportation, power, industry, and residential). The simulated values are compared to surface measurements of AOD, PM_{2.5}, PM₁₀, BC, and OC mass concentrations at the two regional sites in CA. The transport of aerosols into CA is also explored through three-dimensional backward trajectory analysis. Transport from CA and their impacts on downwind areas are also analyzed via forward trajectory analysis. Finally we present results of how the PM concentrations may change in the future using emission scenarios for 2030 that reflect possible air quality and climate policies.

2 Data and methods

2.1 Observations

Surface observations from two sites established in Kyrgyzstan to measure PM concentrations and AOD in CA are used in the analysis. The locations of the Bishkek (42°40'46.65" N, 74°41'38.13" E; elevation 1743 a.s.l.)

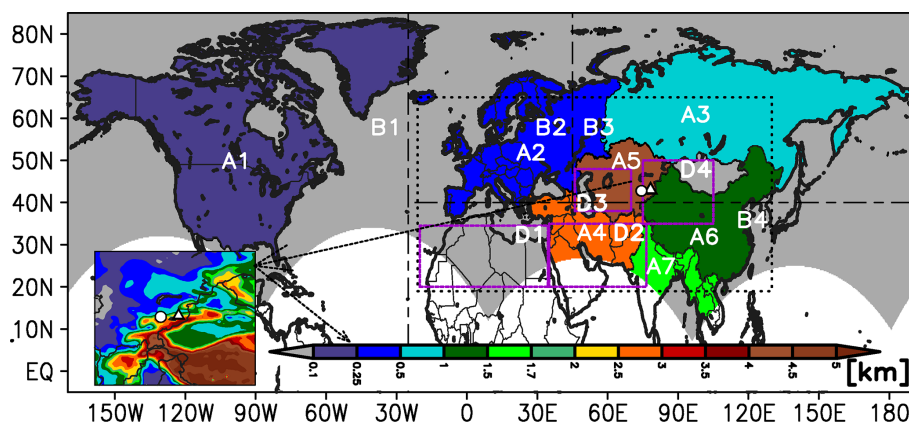


Figure 1. WRF-STEM modeling domain setup and source region definition used in the simulations. Modeling analysis was done on the hemispheric scale. The black dotted rectangular box denotes the subset of the modeling domain used in this analysis. The triangle and circle markers denote locations of the Lidar Station Teplokluchenka (LST) and Bishkek observation sites. The anthropogenic source regions are denoted by colored regions with the A notation: A1 (North America), A2 (Europe), A3 (Russia), A4 (Middle East), A5 (Central Asia), A6 (China), and A7 (South + Southeast Asia). The dust source regions are indicated by the magenta rectangles with the D notations: D1 (Africa), D2 (Middle East), D3 (Central Asia), and D4 (western China). The biomass burning sources regional boundaries are indicated by the long dashed black lines with B notations: B1 (North America, i.e., region west of 25° W), B2 (Europe, i.e., region west of 45° E and 40° N and above), B3 (Siberia: i.e east of 45° E and 40° N and above), and B4 (South Asia, i.e., below 40° N). The insert shows the topography around the observation sites.

and LST (42°27′49.38″ N, 78°31′44.17″ E; elevation 1921 m a.s.l.) sites are denoted by circle and triangle markers, respectively, in Fig. 1. Both sampling sites are in mountain ranges with valleys to the north, with mountains that reach elevations greater than 3500 m a.s.l. south of the Bishkek site and 4600 m a.s.l. south of the LST site, and essentially no population to the south. At each site, PM_{2.5} mass was measured continuously with tapered element oscillating microbalance (TEOM) instruments, and PM_{2.5}, PM₁₀, BC, and OC were obtained using filter-based sampling with samples collected for 24 h every other day. AOD was measured every day at 10:30 LT using Microtops-II sun photometers (SP). A stationary three-wavelength aerosol lidar measured vertical profiles of extinction and depolarization on an event basis at the LST site. The lidar vertical profiles provide information on vertical distribution of the particles, and were also used to calculate AOD from the lidar extinction (LE) profiles and to estimate the height of the planetary boundary layer (PBL) as described in Chen et al. (2013). These observations sites are now part of the UNEP project ABC measurement network (<http://www.ricap.ait.asia/abc/index.cfm>). Further details of the study can be found in Miller-Schulze et al. (2011). Observations from these sites were obtained for the period April 2008 to July 2009 (the TEOM measurements were available from April 2008 and filter measurements began from 1 July 2008).

In addition, the model prediction skill in simulating the aerosols is evaluated using the AOD observations from the AErosol RObotic NETwork (AERONET, available at <http://aeronet.gsfc.nasa.gov/>) located within the domain and the

time period used in this study along with PM₁₀ measurements from the European Monitoring and Evaluation Programme (EMEP, available at <http://www.nilu.no/projects/ccc/emepdata.html>) and the Acid Deposition Monitoring Network in East Asia (EANET, available at <http://www.eanet.asia/product/index.html>) surface site networks. Supplement Table S1 lists the sites from the AERONET, EMEP, and EANET networks used in this study.

The Moderate Resolution Imaging Spectroradiometer (MODIS) collection 5.1 level 2 AOD products (~10 km horizontal resolution) at 550 nm wavelength from Terra and Aqua satellites were used to compare the observed and simulated AOD. The MODIS level 2 data were used and included land and ocean AOD retrieved via the dark-target algorithm (Remer et al., 2005; Levy et al., 2007), and the Deep Blue AOD over land (Hsu et al., 2004, 2006), which can retrieve AOD over bright and desert surfaces. This is particularly relevant for the CA region, which contains major dust sources in western China, South Asia, the Middle East, and Africa (Ginoux et al., 2001). The MODIS level 2 to level 3 averaging procedure outlined in Hubanks et al. (2008) was employed to interpolate the 10 km level 2 AOD products to the 60 km horizontal model resolution on a daily basis. Level 2 QA flag weightings were used to reduce the uncertainty associated with the MODIS retrievals. In grid cells where both the MODIS dark-target and Deep Blue AOD were retrieved, the mean value of the two was used.

2.2 Modeling system

2.2.1 Meteorological model

The Weather Research and Forecasting (WRF) model (Skamarock et al., 2008) version 3.2 was used to generate the meteorological fields needed for simulating the transport patterns in the STEM model (D'Allura et al., 2011). The WRF simulations for each day were initialized using the meteorological boundary conditions obtained from National Centers for Environmental Prediction (NCEP) Final Analysis (FNL, <http://rda.ucar.edu/datasets/ds083.2/>). A daily 24 h spinup time for WRF was used (i.e., WRF was run for 48 h each day and the first 24 h were treated as spinup and were discarded). The STEM model simulation time period was from April 2008 to July 2009.

2.2.2 Chemical transport model

The STEM model (Carmichael et al., 2009) was used to simulate the mass of sulfate, BC, OC, other primary emitted PM_{2.5}, and other primary emitted PM₁₀ (i.e., non-carbonaceous PM such as fly ash, road dust, and cement), which were simulated as a single mass component with aerodynamic diameters less than or equal to 2.5 μm, and between 2.5 and 10 μm (denoted as coarse fraction), respectively, and referred to in this paper as OPM_{2.5} and OPM₁₀, dust (fine and coarse), and sea salt (fine and coarse). Nitrate and secondary organic aerosols (SOA) were not included in the model for this application. The nitrate aerosol is estimated to be a minor component of the PM mass in CA (Baurer et al., 2007). The importance of SOA will be discussed later in the paper. The dry deposition of aerosols was modeled using a resistance-in-series parameterization (Wesely and Hicks, 2000) and wet deposition was calculated as a loss rate based on the hourly precipitation calculated from the WRF model. Further details of the wet scavenging can be found in Adhikary et al. (2007). The modeled AOD at 550 nm wavelength was calculated using the simulated three-dimensional aerosol distributions and species specific extinction coefficients as described in Chung et al. (2010).

2.2.3 Modeling domain

The STEM and WRF computation domains were identical, with a 60 × 60 km horizontal resolution (249 × 249 horizontal grid cells) and 22 vertical layers up to 10 hPa. The domain (Fig. 1) covered much of the Northern Hemisphere in a polar stereographic projection centered over the Arctic region and extended to 35° N to include the major emission regions of North America, Europe, and Asia. This modeling system has been applied to simulate aerosol distributions for ARCTAS field campaign as described in D'Allura et al. (2011) and further details describing the model can be found there. STEM was initialized with a 1-month spinup using March 2008. Much of the analysis for this paper is focused on the

domain denoted by the rectangle centered over CA shown in Fig. 1. This domain has large gradients in topography (insert Fig. 1), which significantly impact the transport patterns in the region.

2.2.4 Air mass trajectories

The CA observation sites are impacted by dust, anthropogenic pollution, and biomass burning emissions from various source regions. To further understand the transport pathways and source region influences on the PM distributions at these sites, three-dimensional 10-day air mass trajectories (both forward and backward in time) from each site were calculated for the entire time period (April 2008–July 2009). In this trajectory analysis, we utilized the three-dimensional wind fields (including *u*, *v*, and *w* components) along with the above ground level (AGL) altitude simulated by the WRF meteorological model consistent with the study of D'Allura et al. (2011). These trajectories describe the general flow patterns based on wind fields alone and provide useful information about the history of air mass, particularly the influence of source regions over which the air mass had resided before arriving at the site of interest. Note that these trajectories do not account for any other atmospheric processes such as diffusion or chemical evolution along its path (Kurata et al., 2004; Guttikunda et al., 2005).

To understand the differences in transport patterns at the surface and aloft, and to study the impact of topographic gradients in the vicinity of the sites, trajectories were initialized at different altitudes (0.1 (100 m), 0.3 (300 m), 0.5 (500 m), 1, 2, 3, and 5 km) above ground level at the site locations (i.e., latitude and longitude) daily every 3 h for a 10-day period both backward and forward in time. The trajectories were terminated when they touched the ground, went out of the model domain, or exceeded the 10-day calculation period. The trajectories (at or below 1 km) were used to characterize transport pathways impacting the surface concentrations at these sites, which are discussed later in Sect. 3.5.

2.3 Emissions

2.3.1 Base emissions

Anthropogenic emissions of BC, OC, PM_{2.5}, PM₁₀, and SO₂ were based on the ARCTAS emissions described in D'Allura et al. (2011), but updated with newly available information. For India and China, BC, OC, and SO₂ emissions from Lu et al. (2011) were utilized, and INTEX-B emissions were used for the rest of Asia (Zhang et al., 2009). For Europe, the EMEP 2008 (<http://www.ceip.at/webdab-emission-database/officially-reported-emission-data>) emissions were used for SO₂, PM_{2.5}, and PM₁₀, and the EUCAARI 2005 inventory was used for the carbonaceous particles (BC and OC) (Visschedijk et al., 2009; Denier van der Gon

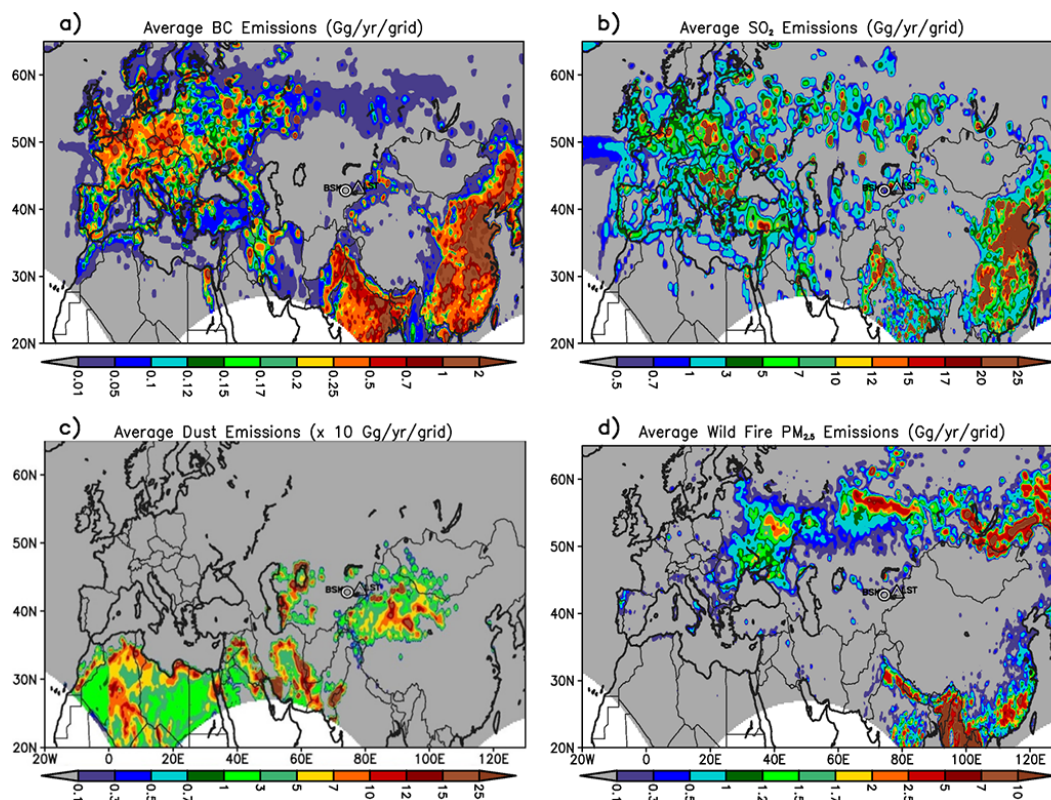


Figure 2. Spatial distribution of (a) BC, (b) SO₂, (c) natural dust, and (d) biomass burning PM_{2.5} emissions averaged over the simulation period in Gg yr⁻¹ grid⁻¹.

et al., 2009). The shipping emissions came from the IIASA base year 2005 inventory (UNEP and WMO, 2011). Mass-conservative regrinding tools including MTX-CALC and MTXCPL from the IOAPI m3tools suite (<http://www.baronams.com/products/ioapi/AA.html#tools>) were used to interpolate the input raw emissions described above onto the model grid.

Anthropogenic emissions for SO₂, BC, and OC were available by major economic sectors, i.e., transportation, residential, industry, and power. The industry and power sectors were treated as small and large point sources, respectively, and emitted into the first six model levels (lowest 2 km). The residential and transportation emissions were treated as near-surface area sources and partitioned into the first two model levels from the surface to ~100 m (i.e., altitude a.g.l of level 2) with a 90:10 percentage split. Monthly emission allocation factors were applied over India and China for the economic sectors from Lu et al. (2011). The rest of the domain (i.e., excluding India and China) used same emission rates for all months due to unavailability of monthly emission allocation factors.

The Fire Inventory from NCAR (FINN v1) was used for BC, OC, CO, SO₂, PM_{2.5}, and PM₁₀ biomass burning emissions from forest, grassland, and crop residual fires. The FINN database, which is based on MODIS fire detection as

thermal anomalies, provides global coverage of fire emissions at a spatial resolution of ~1 km on a daily timescale (Wiedinmyer et al., 2011). The WRF-Chem fire utility (<http://bai.acd.ucar.edu/Data/fire/>) was employed to interpolate the speciated FINN emissions to the WRF model grid. The gridded two-dimensional FINN emissions were used as input to the WRF-Chem (Grell et al., 2005) plume rise model (Grell et al., 2011), which implements the Freitas et al. (2007, 2010) algorithm to compute injection heights and to calculate the vertical distribution of fire emissions at an hourly time step, which were further utilized as input to STEM model simulations.

Sea salt and dust emissions were calculated using the WRF meteorological fields based on the methods described in Gong (2003) and Uno et al. (2004), respectively. The dust emissions were further constrained with snow cover (SNOWC variable from WRF output), and only grid cells with snow cover < 1% were used for dust emission calculations.

Figure 2 shows the annual gridded anthropogenic SO₂ and BC, dust, and biomass burning PM_{2.5} emissions in gigagrams per grid in and around CA. Large BC emission hotspots can be seen over the Indo-Gangetic Plain and eastern China. Significant BC emissions are also seen over Europe, but they are relatively lower in intensity than the Asian sources. The SO₂

emissions show eastern China as the largest source region, followed by regions of South Asia, Europe, and Russia. The major natural dust emission sources (Fig. 2c) include Africa, the Middle East, CA, western Indian boundaries, and western China. The major sources of biomass burning are eastern Europe, portions of Siberia (between 40 and 60° N), Southeast Asia, southern China, and India (Fig. 2d).

Dust emissions have a strong seasonal cycle. The major dust sources in the region (Fig. 1) are located to the east, west, and south of the observation sites and include the cool winter deserts around the Aral and Caspian seas and those in western China and northern Pakistan, as well as the subtropical deserts in western India, around the Persian Gulf, and northern Africa. The emissions from the cool winter deserts occur when the surfaces are free of snow cover (from March through October). Emissions from the subtropical deserts can occur throughout the year.

The open biomass burning emissions that impact CA also have a strong seasonality with minimum impact in winter (Supplement Fig. S1). Fires typically begin in the spring in Siberia along 50° N latitude and in northern India and Southeast Asia and in summer the high-latitude burning shifts to the west. In October the fire activity decreases and remains low until spring, with the most active fire regions associated with agricultural burning in northern India and southeastern China.

2.3.2 Future emissions scenarios

In addition to the base emissions, a series of simulations were analyzed using emission scenarios for 2030. These scenarios were developed for the WMO/UNEP report that looked at short-lived climate pollutants as described in Shindell et al. (2012) and Anenberg et al. (2012). The reference scenario for 2030 was based on the implementation of control measures currently approved in the various regions and assumed their perfect implementation. The 2030 reference scenarios were developed from a reference global emissions inventory with a 2005 reference year, and assumed significant growth in fossil fuel use relative to 2005, leading to increases in estimated CO₂ emissions (45 %). Abatement measures prescribed in current legislation were projected to lead to reductions in air pollutant emissions, which varied by pollutant and region. In the 2030 reference scenario, total primary PM_{2.5} emissions remain approximately constant, while BC and OC decline by a few percent. However, in the study domain, emission changes varied widely. BC emissions increased by 10–100 % in CA, South and Southeast Asia, and western China, and decreased in East Asia and Europe. The PM_{2.5} emissions showed similar regional changes but grew at lower rates (10–40 %). SO₂ emissions generally increased throughout the region by 10–20 %. Spatial maps of emission changes for the 2030 reference scenario are presented in Figs. S2b, S3b, and S4b.

A series of emission control scenarios for 2030 were developed to evaluate the impact of additional abatement measures designed to reduce the levels of short-lived climate pollutants (e.g., BC). The BC measures in the scenarios included two different sets of assumptions (low and lowest). The first focused on reductions from incomplete combustion sources. These included implementation of Euro 6-equivalent vehicle emission standards (requiring installation of diesel particulate filters) and improving traditional biomass cook stoves in developing countries (assuming a 25 % decrease in BC and 80–90 % decreases in OC, CO, non-methane volatile organic compounds (NMVOC), methane, and direct PM_{2.5} relative to emissions from traditional stoves). Under this scenario BC and PM_{2.5} emissions in the study region are projected to decrease throughout most of the domain, with SO₂ emissions showing almost no change (see Figs. S2c, S3c, and S4c).

The lowest option assumed the additional elimination of high-emitting vehicles, biomass cook stoves (in developing countries), and agricultural waste burning. These BC measures in the lowest scenario reduced global anthropogenic BC emissions by 75 %. Measures targeting BC also substantially reduced total primary PM_{2.5} (–50 %), OC (–79 %), NO_x (–27 %), and CO (–44 %). These BC measures have little impact on SO₂ emissions. Projected emissions of BC and OC under these scenarios are reduced most in Asia, followed by Africa, North America, and Europe.

These measures were also combined with a scenario designed to stabilize greenhouse gases at 450 ppm of CO₂ equivalent (lowest + 450 ppm scenario), consistent with a global average temperature increase of ~2°C. These CO₂ measures reduced SO₂ (–30 %) (Fig. S4d) and NO_x (–20 %), but had little further impact on BC (~5 % decline, Fig. S2d) since the major sources of CO₂ differ from those of BC. PM_{2.5} emissions were substantially further reduced under this scenario (Fig. S3d).

2.4 Simulations analyzed

The CA region is strategically located and aerosols at these sites are shown to reflect impact of varied dust (including CA, western China, Africa, and the Middle East), biomass burning (including Europe, Siberia, South Asia and North America) and anthropogenic sources (including Europe; South, East, and Central Asia; and Russia) depending on the time period. Therefore we choose different regions for the anthropogenic, dust, and biomass burning in order to capture the impact and the associated seasonality of these main regions on the regional distribution of aerosols in this region. As a result we have more anthropogenic regions to better understand how regional changes in emissions may impact CA PM levels.

Several simulations were analyzed for this paper. The base simulation included all sources and used the meteorology from the WRF model for the period April 2008–July 2009. To investigate the contributions from specific source sec-

tors, additional simulations were performed where emissions from one sector were set to zero everywhere. The contribution from each sector was calculated as the difference between the base simulation and the simulation with emissions from that particular sector set to zero. This was repeated for each sector and for biomass burning. Additional simulations were performed to assess the source contribution from specific regions to the particle levels in CA. The specific regions used are shown in Fig. 1. In these simulations all anthropogenic emissions were set to zero in that region. In a similar manner, regional dust and fire sources were also studied, and the source regions are also shown in Fig. 1. Finally, simulations were performed using the reference 2005 and 2030 emissions and the low and lowest + 450 CO₂ 2030 scenarios (described above). For these runs, the meteorology, open biomass burning, and dust emissions were the same as in the base run (i.e., 2008/2009).

2.5 Model evaluation

We have evaluated this model framework in other regions outside CA, including the Arctic region and continental USA previously, which are summarized below. The domain configuration and settings of the WRF/STEM modeling system used in this study have been applied to provide meteorology and air quality forecasting during the ARCTAS field campaign in 2008 (D'Allura et al., 2011) as mentioned earlier in Sects. 2.2.3 and 2.3.1, respectively. The study by D'Allura et al. (2011) used WRF v2.2 and pre-emission ARCTAS emissions data (http://mic.greenresource.cn/arctas_premission), real-time biomass burning emissions from the RAQMS modeling group (<http://raqms-ops.ssec.wisc.edu/>) and evaluated the performance of the WRF-STEM modeling framework (used in this study) through the case study of the ARCTAS mission DC-8 flight conducted on 9 July 2008. The WRF model compared well with observed meteorological variables (including temperature, pressure, wind speed, and wind direction) along the flight and correctly simulated the various meteorological processes (i.e., cyclonic circulation, low-pressure system, anticyclones, and geostrophic wind flows) that facilitate transport of pollutants into the Arctic region. This study also compared CO along the flight and found that the simulated values were able to capture the magnitude and temporal variability seen in observed values. The study also found that the fires from North Asia and anthropogenic CO from China were the major sources contributing to observed CO levels along the flight, suggesting that the midlatitude pollution and summertime forest fires/biomass burning transport events were well represented in this modeling system.

Huang et al. (2012) used a subset of this domain (covering the region of continental North America) to simulate summertime sectoral and regional contributions to BC over continental USA using the WRF/STEM modeling framework. Note that the study of Huang et al. (2012) used the same WRF meteorology, ARCTAS emissions, and RAQMS

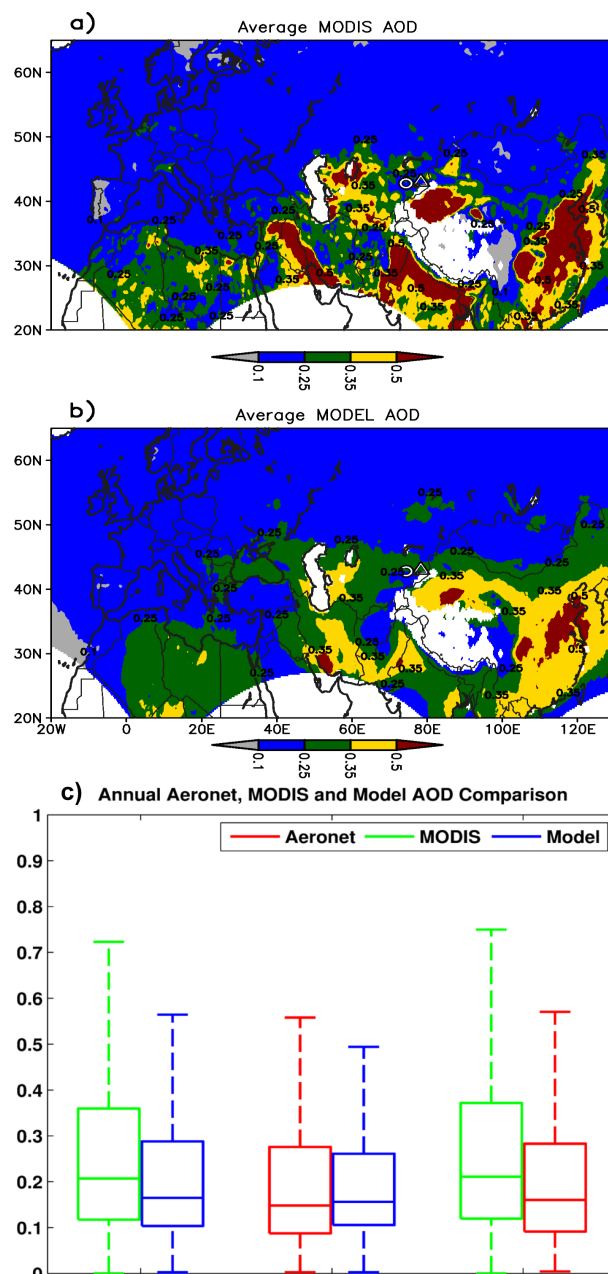


Figure 3. Spatial distribution of (a) MODIS and (b) modeled AOD along with (c) comparison of MODIS, AERONET, and simulated AOD shown as box-and-whisker plots averaged over the simulation period. The box plots are based on data that are paired in time and space (see Sect. 3.2.1 for more details). The triangle and circle markers on the spatial plots denote the location of LST and Bishkek sites. The numbers on the map denote contour values at sharp gradients. In each box-and-whisker panel, the middle line denotes the median value, while the edges of the box represent 25th and 75th percentile values, respectively. The whiskers denote the maximum and minimum values.

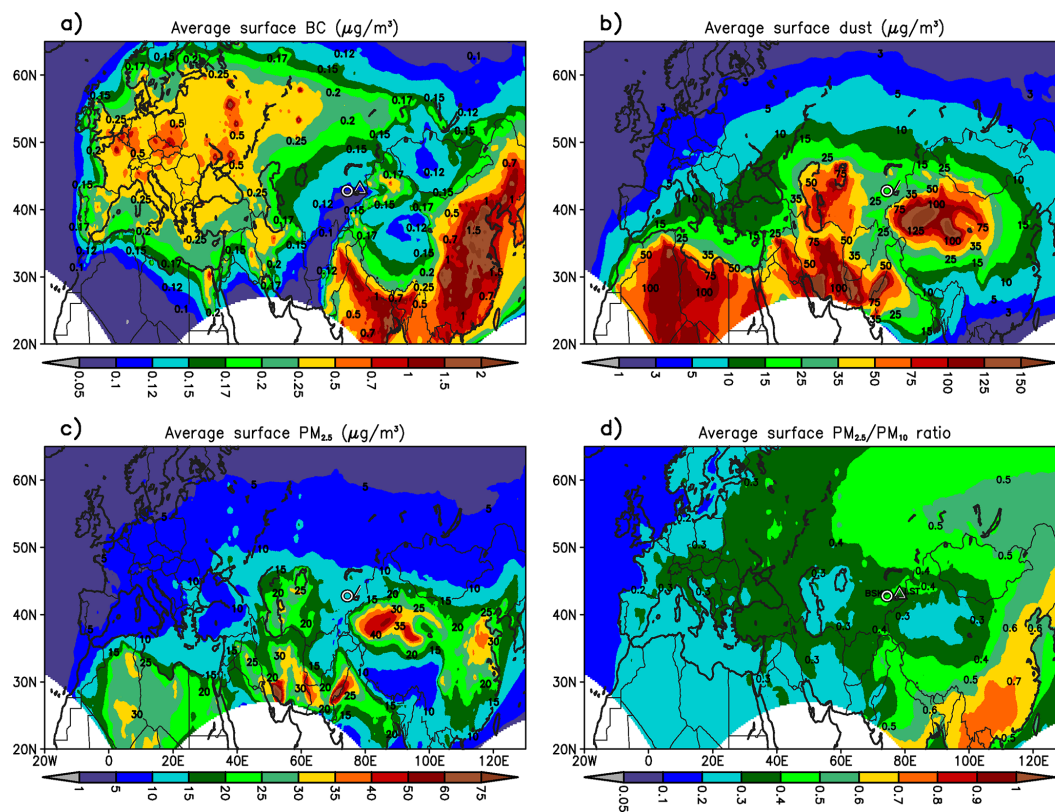


Figure 4. Spatial distribution of simulated (a) BC ($\mu\text{g m}^{-3}$), (b) dust ($\mu\text{g m}^{-3}$), (c) PM_{2.5} ($\mu\text{g m}^{-3}$), and (d) PM_{2.5}/PM₁₀ ratio averaged over the simulation period. The values on the map denote contour values at sharp gradients.

biomass burning emissions used in the D'Allura et al. (2011) but used the full-chemistry version of the STEM model. The comparison of the simulated aerosol BC from the STEM tracer model with corresponding BC values from the full-chemistry version of the STEM model showed that the simulated tracer BC was able to capture trend and the same relative variability seen in the full-chemistry predictions. Huang et al. (2012) evaluated the model performance aloft and at surface using measurements from ARCTAS mission DC-8 flights conducted on 20, 22, and 24 June and that sampled over California and IMPROVE surface site network. Huang et al. (2012) found that the predicted BC values captured many of the vertical features seen in the flight observations with a tendency to overpredict surface BC and >4 km. The comparison of predicted BC with observed values from the IMPROVE network showed that the model was able to capture the gradients in BC values with high concentrations in western and eastern NA regions with slight positive and negative biases over the mountain regions and the eastern USA/California. In this paper we further evaluate the performance of the model over the selected domain in this study (Fig. 1) using MODIS and AERONET AOD and PM₁₀ surface observations as described in the following sections.

3 Results and discussion

3.1 Regional perspective

CA is a region with high aerosol loadings as shown in the mean MODIS-retrieved AOD at 550 nm for the time period of study (April 2008–July 2009) (Fig. 3a). AOD (period mean) throughout CA (~ 45 – 90°E , 35 – 50°N) are greater than 0.25, with the highest regional values around the desert areas near the Caspian and the Aral seas. There are also high values (>0.6) along CA's eastern border, which reflect the deserts and rapidly developing cities in western China, and to the south over Pakistan and northern India.

The period mean predicted surface concentrations of PM_{2.5}, BC, total dust (fine and coarse), and PM_{2.5}/PM₁₀ ratio are shown in Fig. 4. The BC levels in CA are typically less than $0.3 \mu\text{g m}^{-3}$ and its spatial pattern reflects contributions from both anthropogenic and biomass burning sources (Fig. 4a). The simulation period mean PM_{2.5} concentrations in CA (10 to $35 \mu\text{g m}^{-3}$) (Fig. 4c) have a similar geographical distribution as AOD (Fig. 3a). Dust is the major component of predicted PM₁₀ in CA as seen from the high dust concentrations (25 – $100 \mu\text{g m}^{-3}$) in Fig. 4b and low values (0.3 – 0.4) of the predicted PM_{2.5}/PM₁₀ ratio (Fig. 4d). The natural dust source regions including western China, the Middle

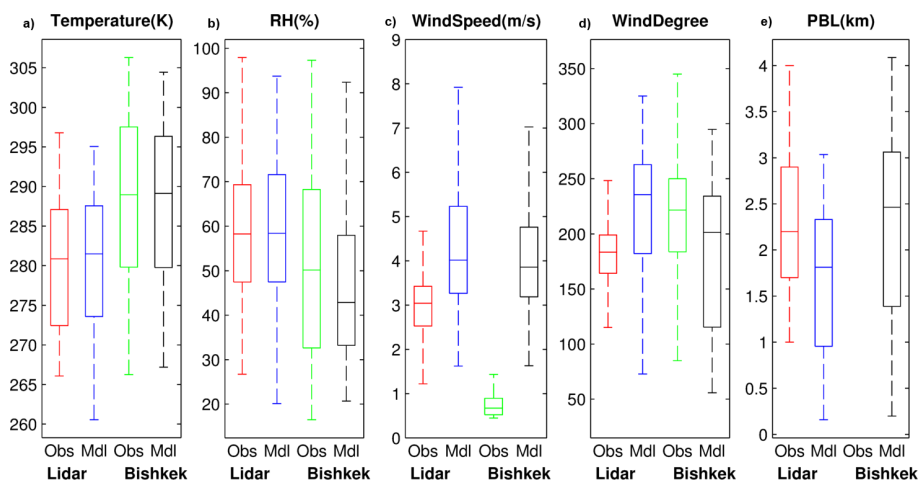


Figure 5. Comparison of predicted meteorological variables from WRF model with observations shown as box-and-whisker plots over the simulation period **(a)** temperature (K), **(b)** relative humidity (RH, %), **(c)** wind speed (m s^{-1}), **(d)** wind direction ($^{\circ}$), and **(e)** PBL height (m). “Lidar” denotes the LST site. In each box-and-whisker panel, the middle line denotes the median value, while the edges of the box represent 25th and 75th percentile values, respectively. The whiskers denote the maximum and minimum values.

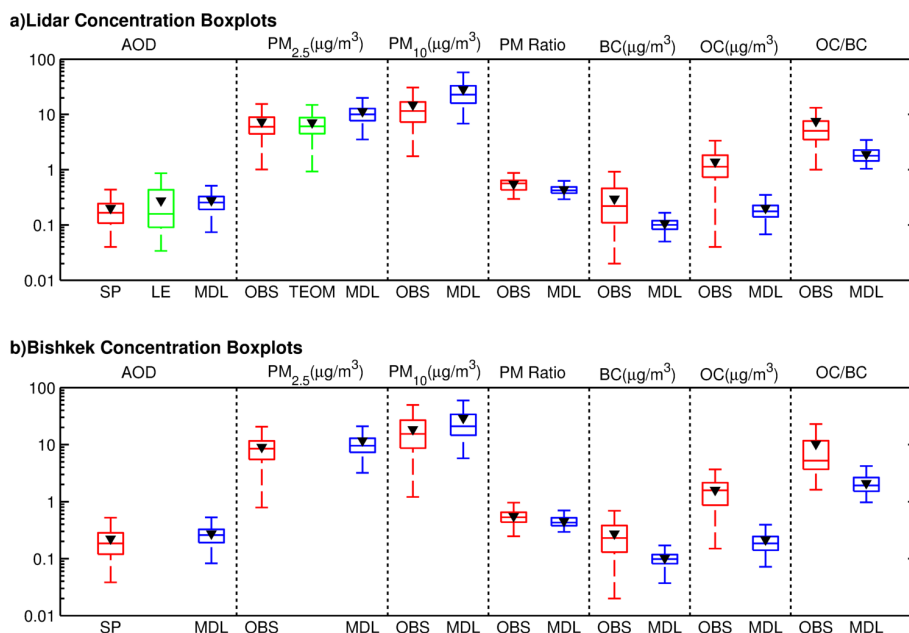


Figure 6. Comparison of predicted aerosols with observations shown as box-and-whisker plots over the simulation period at **(a)** LST and **(b)** Bishkek sites. SP and LE denote the AOD from the sun photometer (SP) and integrated from the vertical extinction profiles (LE). OBS and TEOM denote filter and TEOM measurements, while the MDL denotes the modeled values, respectively. “Lidar” denotes the LST site. In each box-and-whisker panel, the middle line denotes the median value, while the edges of the box represent 25th and 75th percentile values, respectively. The whiskers denote the maximum and minimum values. The triangle marker denotes the mean value.

East, Africa, and western India have similar $\text{PM}_{2.5} / \text{PM}_{10}$ ratio values (0.3–0.4), reflecting the major contribution of dust to PM over these regions. The high predicted $\text{PM}_{2.5} / \text{PM}_{10}$ ratio values (> 0.6) are seen over southern and eastern China indicate that the non-dust sources are the dominant contributors to PM in this region.

3.2 Model evaluation with AOD and PM measurements

3.2.1 Comparison with MODIS and AERONET AOD

The predicted period mean AOD spatial distribution is shown in Fig. 3b (using only data from grid cells where MODIS AOD was available; the white-colored areas denote regions

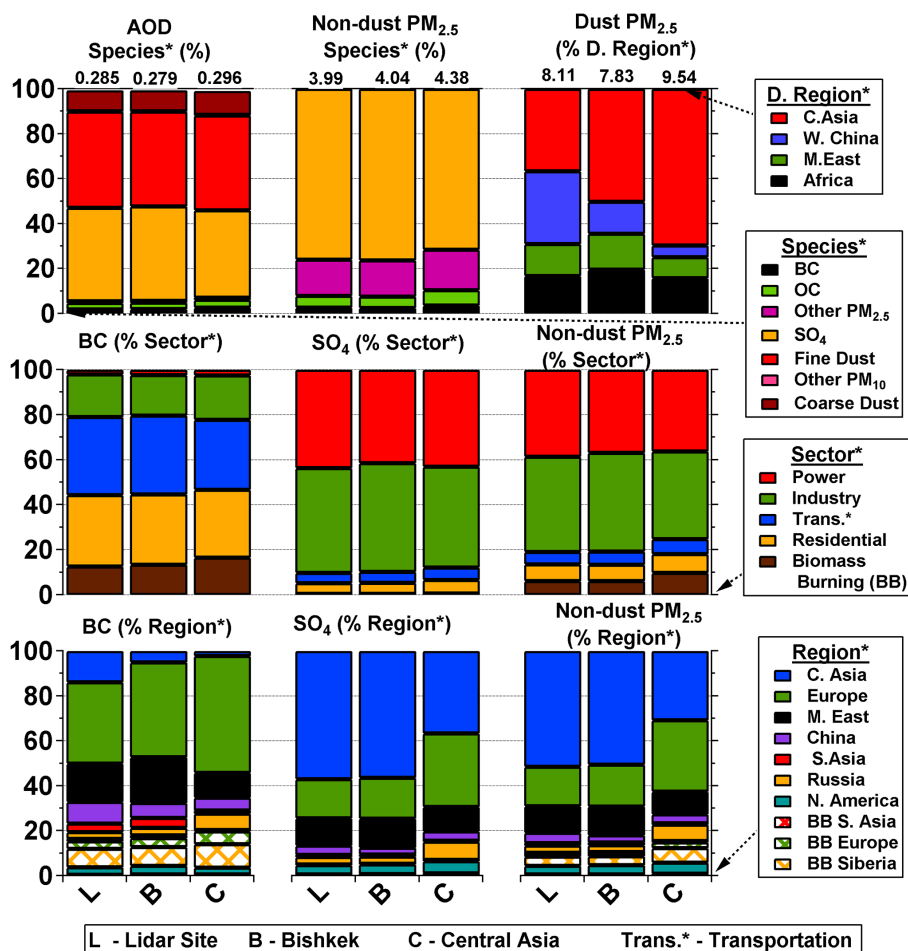


Figure 7. Summary of period mean contributions by source regions and sectors for AOD, PM_{2.5}, dust, non-dust PM_{2.5}, sulfate, and BC in percent for the grid cells containing the Bishkek and LST observation sites, and spatially averaged over the Central Asia region. See Fig. 1 for anthropogenic, dust, and fire source regions. “Lidar” denotes the LST site.

where MODIS AOD data were not available). The simulated AOD values capture the main observed spatial features – including enhanced AOD over desert regions of Asia (i.e. East Asia, West Asia and along the western border of India) and regions that are known to have large impacts from anthropogenic and wildfire emissions (i.e. eastern China, northern India covering the Indo-Gangetic Plain and Southeast Asia). However, the period mean AOD values are biased low relative to MODIS AOD over the regions of northern India and eastern China. This could be in part related to uncertainty associated with anthropogenic emissions over these regions and the 60 km model resolution used in this study. The simulated AOD values are overpredicted relative to MODIS AOD over regions surrounding CA, including parts of eastern Europe, Russia, northern China, western Asia, and Africa. These biases could be partly attributed to the uncertainty associated with regional transport of dust shown in spatial patterns of simulated dust and PM_{2.5}/PM₁₀ ratio (Fig. 4b and d).

The model prediction skills in simulating the temporal and spatial patterns in AOD was evaluated by comparing the predicted daily AOD with the corresponding measured Level 2 AOD values at 142 sites from the AERONET program (see Table S1 for AERONET site details) located within the domain and for the time period used in this study. We have also compared the AERONET AOD with MODIS on a daily timescale by extracting the daily MODIS-retrieved AOD corresponding to the AERONET site locations for the simulation time period. The comparison of the predicted daily AOD with the available MODIS retrievals ($n = 29680$ using MODIS and simulated AOD extracted at the AERONET site locations, which are paired in space and time) is shown in Fig. 3c. The model values show a similar mean value (average simulated and MODIS AOD are 0.24 and 0.31, respectively), with a negative bias and an underprediction in the variability. The comparison of model predictions with respect to AERONET AOD data ($n = 22\,875$) shows much closer agreement with mean modeled and AERONET val-

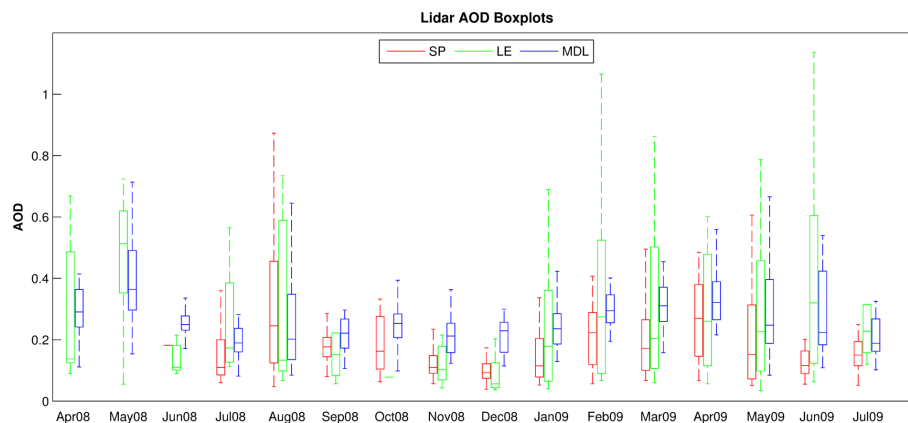


Figure 8. Temporal variability in simulated AOD compared with observations at the LST site. The box plots of monthly values are shown. AOD from the sun photometer (SP) and integrated from the vertical extinction profiles (LE) are shown. MDL denotes modeled values. “Lidar” denotes the LST site. In each box-and-whisker panel, the middle line denotes the median value, while the edges of the box represent 25th and 75th percentile values, respectively. The whiskers denote the maximum and minimum values.

ues of 0.21 and 0.23, respectively (note the comparison is based on paired data for the times only when AERONET data were available so that the means are different than the MODIS–model comparison). Also shown is the comparison between MODIS and AERONET (for times/locations with paired AERONET measurements; $n = 12\,719$) with AERONET and MODIS mean values of 0.24 and 0.29, respectively. The comparison results of AERONET with respect to MODIS are similar to corresponding values of the MODIS–model comparison, indicating that MODIS retrievals are biased high in the study domain. A more detailed analysis of the AOD comparison by region and season is included in the Supplement (Table S2 and Figs. S5 and S6).

3.2.2 Comparison with PM₁₀ observations from EMEP and EANET network

We also evaluated the simulated PM₁₀ values with monthly mean observed data for the simulation time period from the EANET network over Asia (see Fig. S7). The modeled values are underpredicted as evident from the mean observed and modeled PM₁₀ values of 32.2 and 22 $\mu\text{g m}^{-3}$ ($n = 314$). The normalized mean bias and error are $\sim -32\%$ and 44 %, respectively. This could be partly attributed to the uncertainty associated with dust emissions that have a significant impact on the EANET site locations (see Table S1 for PM₁₀ site locations). We also evaluated the simulated PM₁₀ values over Europe using the available monthly mean observations from EMEP for the 2002–2003 time period (see Table S1 for EMEP PM₁₀ site locations). The mean observed and modeled values of PM₁₀ are respectively 23.9 and 22.2 $\mu\text{g m}^{-3}$ ($n = 130$). The normalized mean bias and error for the EMEP PM₁₀ are -7 and 43 %, respectively, suggesting an overall underprediction by the model.

The evaluation of this model framework in other regions outside CA, including the Arctic region and continental USA (described earlier in Sect. 2.5), along with the comparison of regional distribution and temporal variability in simulated AOD using corresponding MODIS and AERONET measurements indicates that the predictions of aerosol mass and composition at the hemispheric scales are able to capture important aspects of horizontal gradients and variability but have considerably higher uncertainties associated with emission estimates (in particular forest fires/biomass burning and natural dust emissions) and wet removal processes (Bates et al., 2006).

3.3 Comparison with surface observations in CA

The surface observations at the two CA sites provide the opportunity for the first time to evaluate the performance of chemical transport models in estimating the distribution of aerosols in CA and to assess the emission estimates in the region. A comparison of the predicted and observed meteorology is presented in Fig. 5, where the distributions of key meteorological parameters for the entire measurement period are shown as box plots. The model accurately predicted the magnitude and variability in temperature and relative humidity. For example, the model mean values of temperature and relative humidity are 279.3 K and 61.6 % in comparison to the observed values of 280.3 K and 59.2 % at the LST site. The model wind speeds were biased high by about 30 % (mostly in winter; see Sect. 3.4) and the direction had a southwest bias. These biases are due in part to the 60 km model grid size, which is too coarse to capture the steep gradients in topography in and around the observation sites, and to the site placement in small N–S-oriented valleys. More details regarding the evaluation of the modeled meteorology can be found in Table S3 in the Supplement.

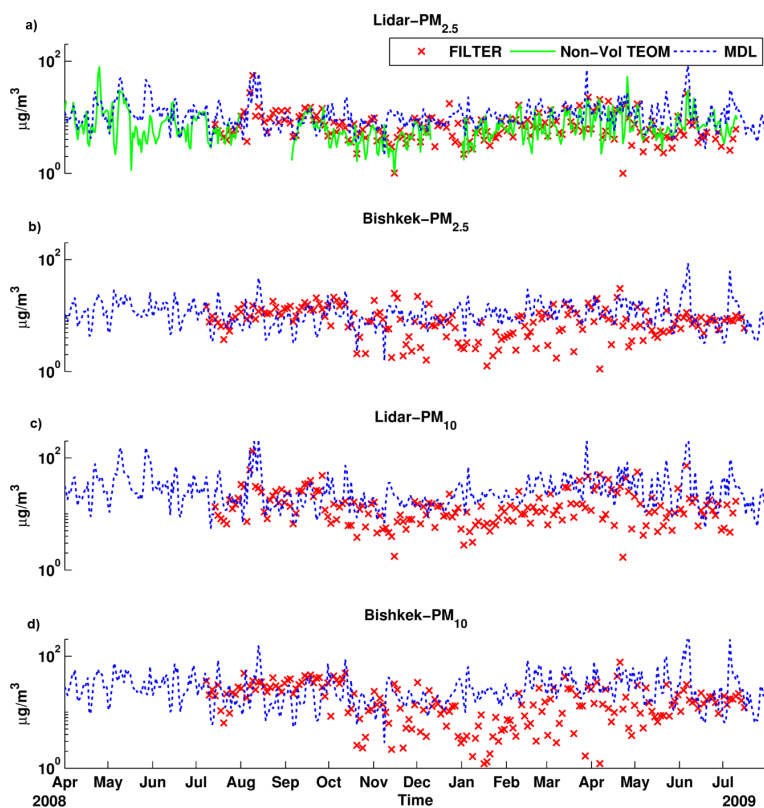


Figure 9. Comparison of simulated PM mass with filter-based observations at Central Asian sites. (a) PM_{2.5} (LST) along with TEOM non-volatile measurements, (b) PM_{2.5} (Bishkek), (c) PM₁₀ (LST), and (d) PM₁₀ (Bishkek) in ($\mu\text{g m}^{-3}$). “Lidar” denotes the LST site.

The observed and modeled distributions of AOD and PM are compared in Fig. 6. The AOD observations based on the LE on average are $\sim 50\%$ larger than those from the SP. Modeled AODs are on average $\sim 20\text{--}30\%$ higher when compared to SP at the Bishkek and LST sites and $\sim 1\%$ lower when compared to the LE values. The variability in the predictions is slightly underestimated. PM_{2.5} is overpredicted ($\sim 50\%$) and the spread is accurately captured, while PM₁₀ is overpredicted by $\sim 70\%$. This leads to an underestimation of the PM_{2.5}/PM₁₀ (0.4 predicted versus 0.5 observed) and also helps account for the overestimation in modeled AOD (by $\sim 20\text{--}30\%$).

Chemical analysis of the filter and soil samples in the CA dust regions have been used to estimate the dust contribution to measured PM at the two sites and to help identify source regions of importance. The emission regions within CA, including around the Aral Sea, and western China were identified as the most important dust sources, which is consistent with the regions identified in the simulations. Dust was estimated to comprise between 5 and 40 % of PM_{2.5} mass at the LST site and to vary by season (minimum values in winter). The observation-based estimates of dust percentage contribution suggest that modeled dust is overpredicted by a factor of ~ 2 . Thus it appears that dust is a main reason for the over-

prediction of PM_{2.5} and PM₁₀, and that dust emission models need to be refined for CA applications.

The overestimation in PM mass at the surface could also be impacted by errors in the modeled PBL heights. The PBL height as determined by the lidar aerosol profiles varies seasonally and is highest in the summer (from 2 to 4 km a.g.l.) and lowest in the winter (November–February, 0.5–1.5 km a.g.l.) (Fig. S5). The predicted PBL heights show a similar seasonal cycle with a tendency to underpredict the heights in all seasons as indicated by the comparison of the distributions of the observed and predicted values (Fig. 5), and this occurs in all seasons (Fig. S8). The lower PBL height in the model contributes a systematic high bias in surface concentrations driven by near-surface emissions. Further statistical details of the model–observation comparison can be found in the supplemental materials (Table S4). The seasonal variability in the observations is discussed in further detail later (Sect. 3.4).

3.4 Source contributions to PM_{2.5}

Model simulations were performed to identify the component, source region, and emission sector contributions to PM_{2.5} mass. Period means for the spatial average over the entire CA region (see Fig. 1) and for the grid cells for

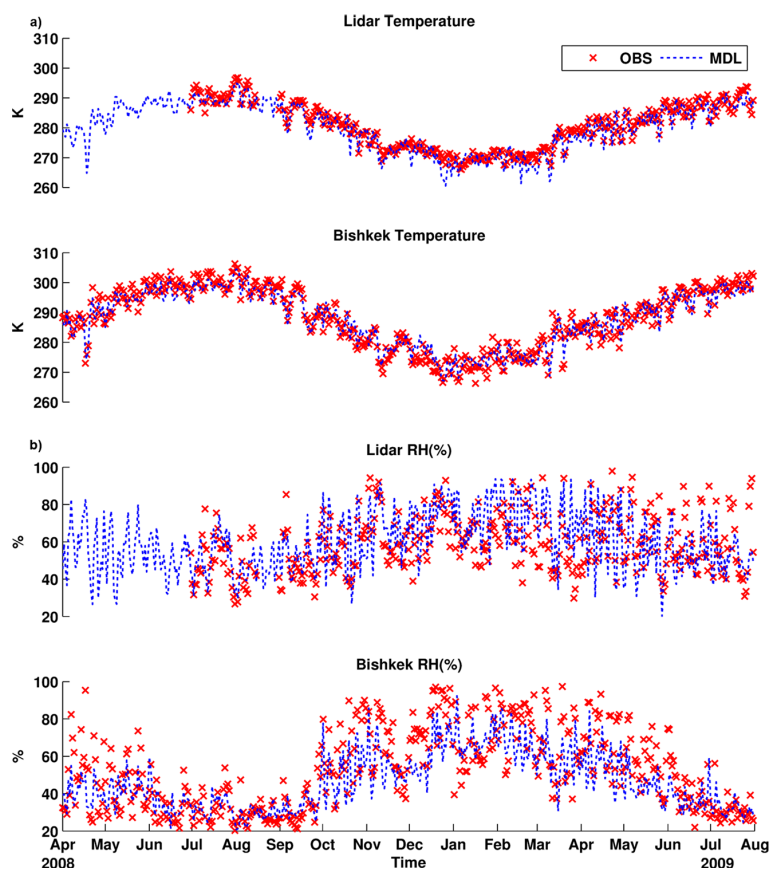


Figure 10. Temporal variability in simulated (a) temperature (K) and (b) relative humidity (RH, %) from the WRF model compared with observations at the LST and Bishkek sites. “Lidar” denotes the LST site.

the Bishkek and LST observation locations are presented in Fig. 7, and their comparison provides insights into the spatial variability of PM and its sources within CA as well as how representative the observation sites are at characterizing CA PM. The component contribution to AOD at the sites and for the CA average are similar, with the major contributions coming from fine dust, sulfate, and OC. Spatial maps of mean percent contributions of the various components (i.e., BC, OC, sulfate, OPM, dust, and sea salt) to AOD and PM_{2.5} mass are presented in Figs. S9 and S10, respectively. Coarse particles contribute ~ 10 % to mean AOD. Dust accounts for > 60 % of the calculated PM_{2.5} mass at the observation sites and for the CA region. The dust source regions (see Fig. 1) contributing to PM_{2.5} vary within CA. Dust from the CA source regions has the largest influence on the region mean dust PM_{2.5} mass. At the LST site, which is located in the far east of CA, western China dust sources have their largest influence (~ 40 %). African and Middle Eastern source regions have their largest influence on the Bishkek site (20 and 15 %, respectively), and collectively contribute ~ 25 % to regional CA dust PM_{2.5}.

The source region contributions to the non-dust PM_{2.5} are very similar for the Bishkek and LST sites, with CA

sources making the largest contribution (~ 50 %), followed by Europe (~ 20 %), the Middle East (~ 15 %), and biomass burning (~ 15 % from all sources). For the entire CA region the European source contribution is as large as the CA sources (~ 30 % each), with larger contributions from biomass burning and Russian sources and smaller contributions from Middle Eastern emissions than at the observation sites. The significant contribution from European sources reflects their large anthropogenic emissions and the general westerly transport patterns. On average the impact from South Asian sources is small. North American sources contribute between 3 and 7 % to PM_{2.5} in CA. Of the biomass burning contribution to PM_{2.5}, the Siberian and European fires (see Fig. 1 for fire regions) contribute 63 and 25 %, respectively, with contributions from South/Southeast Asian and North American fires each contributing ~ 5 %. The power and industrial sectors are identified by the simulations as the largest contributors (~ 40 % each) to non-dust PM_{2.5} mass in CA.

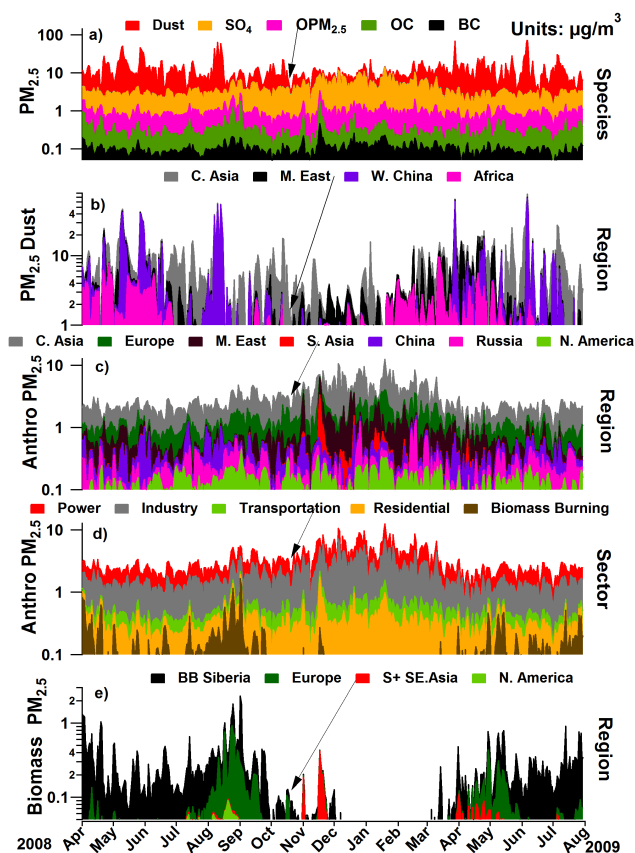


Figure 11. Simulated composition of PM_{2.5} at the LST site by (a) species ($\mu\text{g m}^{-3}$), (b) fine dust source regions ($\mu\text{g m}^{-3}$), (c) anthropogenic PM_{2.5} source regions ($\mu\text{g m}^{-3}$), (d) anthropogenic PM_{2.5} source ($\mu\text{g m}^{-3}$), and (e) biomass PM_{2.5} source regions ($\mu\text{g m}^{-3}$). The contributions from source region and sectors denote the non-dust portion of PM_{2.5} mass.

3.5 Seasonal variations in AOD and PM at the observation sites

AOD has a seasonal cycle with the lowest values in winter and highest values in spring and summer as shown in Fig. 8 by the AOD observations at the LST site from both the SP and the LE profiles. A similar seasonal cycle was observed at the Bishkek site (not shown) and in the MODIS AOD retrievals (Fig. S11). The modeled AOD captures this seasonal variation, with a tendency to overpredict the values during the periods with the lowest observed AOD.

The seasonal cycles in PM_{2.5} (Fig. 9) and PM₁₀ are similar to those for AOD, with minimum values in October–February. At the LST site, PM_{2.5} from both the filter-based and non-volatile TEOM measurements is plotted. Both the observations and the model find a strong similarity in the time series at the two sites.

There is also a clear seasonality in the surface meteorology in the region as shown by the time series in surface temper-

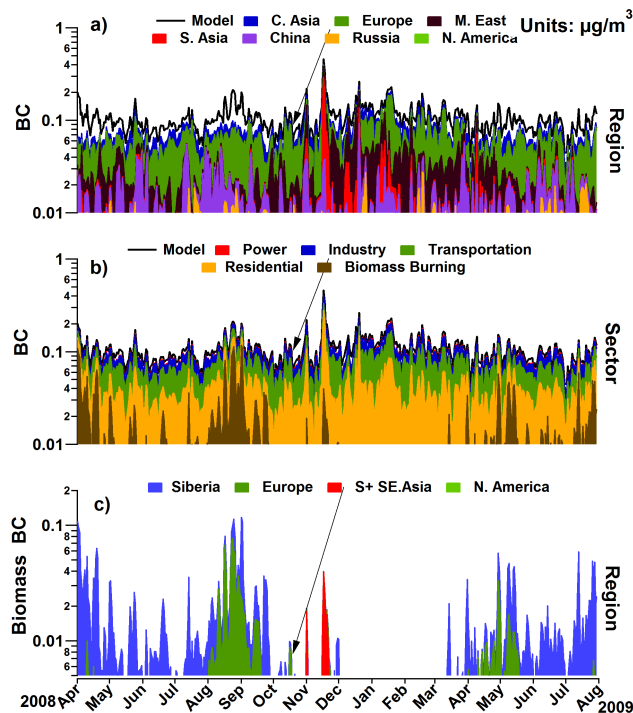


Figure 12. Simulated composition of BC at the LST site by (a) source regions ($\mu\text{g m}^{-3}$), (b) source sector ($\mu\text{g m}^{-3}$), and (c) biomass burning source regions ($\mu\text{g m}^{-3}$).

ature and relative humidity at the two sites (Fig. 10). There are distinct temperature minima in the winter and relative humidity minima in the summer. However there is not a clear seasonality in wind speed and direction, and the winds are generally from the south and less than 4 m s^{-1} throughout the year at the LST site (not shown).

The source region and component contributions exhibit seasonal variability as shown by the modeled contributions to PM_{2.5} mass in Fig. 11. Dust is found to be the main driver of the seasonal cycle of PM_{2.5}. The dust contribution to PM_{2.5} is peak in spring and minimum in winter ($< 20\%$). During this time period the transport of air masses to the sites are from the west and the southwest. When the transport is from the east, then dust sources from western China can impact the stations. This transport pattern occurs episodically throughout the year, with contributions from western China sources as large as 20 to 50%. The dust seasonal cycle is in turn influenced by the seasonal variations in meteorology that drive the dust emissions and transport. The seasonal changes in the dust source regions can be seen in the seasonal spatial maps of AOD (Fig. S11). Throughout the domain, AODs in the dust regions are highest in March–October and lowest in winter (Fig. S11) as the nearby desert regions are snow covered.

Biomass burning also adds to the seasonal cycle, and its contribution is minimum in the winter. South Asian sources can impact the sites in the winter time. The periods when

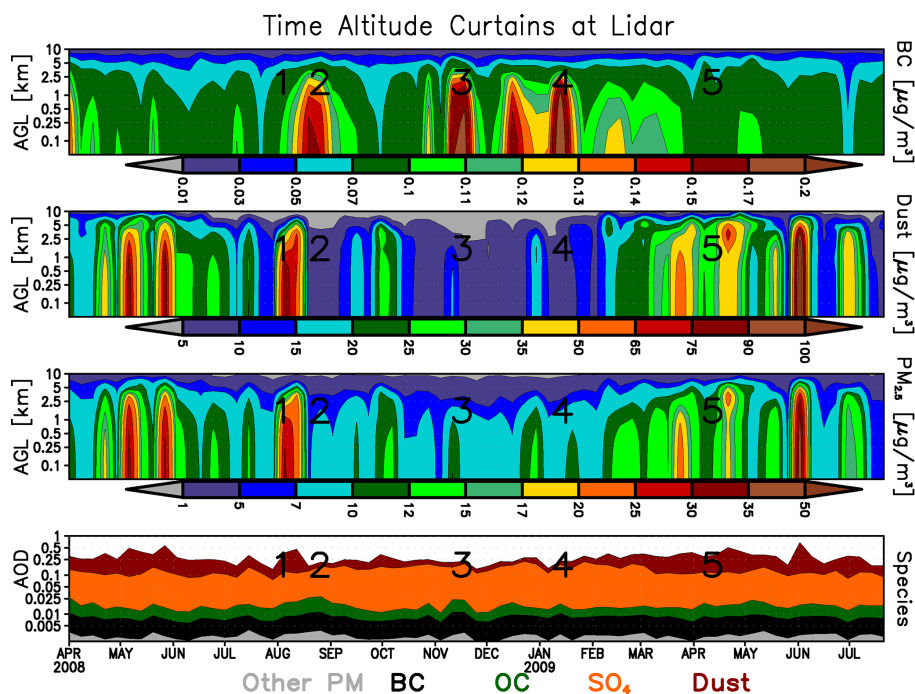


Figure 13. Time–altitude cross sections of weekly averaged predicted BC, dust, and PM_{2.5} for the simulation period at the LST site. The numbers denote the specific episodes of aerosol enhancements for back trajectory analysis in Figs. 14 and 15. “Lidar” denotes the LST site.

North American sources impact the site are associated with strong transport events across the Atlantic and subsequent subsidence towards the surface associated with high-pressure systems as they move towards CA. The transport pathways are discussed in more detail in Sect. 3.7.

3.6 Source contributions to BC

Because of BC’s dual role as an air pollutant and as a climate warming agent, there is special interest in understanding the regional and sector contributions to it (Ramanathan and Carmichael et al., 2008). BC comprises on average only about 1–2 % of PM_{2.5} mass in CA. The period mean predicted BC surface concentrations are $\sim 0.1 \mu\text{g m}^{-3}$ at the two observation sites and $0.15 \mu\text{g m}^{-3}$ for the CA regional average. As shown in Fig. 7, European emissions contribute $\sim 50\%$ to the mean BC concentrations in CA, while Middle Eastern and biomass burning sources each contribute $\sim 15\text{--}20\%$. Residential and transport are the most important sectors, each contributing $\sim 30\%$ to BC in CA, followed by industry ($\sim 20\%$), and with power the least important. This is in contrast to the sector contributions to non-dust PM_{2.5} mass, where power and industry are the most important sectors. On average, biomass burning contributes $\sim 10\%$ to BC mass, with Siberian and European fires accounting for 61 and 33 %, respectively. The source contributions to OC are shown in Fig. S12.

There is also large seasonal variability in BC concentrations and source sector/region contributions (Fig. 12). BC

surface concentrations show the highest values in fall/winter (as do the observations), when there is maximum contribution from the residential sector, reflecting the widespread use of biofuels and coal for heating in the region. The source region contributions vary by season, with maximum contributions from Europe and China. South Asian sources contribute in the winter. Biomass burning also is an important source of BC and plays an important role in influencing daily and seasonal variability in BC concentrations.

Predicted BC captures the seasonality and the magnitude of the spring and summer values as observed, but concentrations are biased low in the fall/winter. Median BC concentrations (and variability) are underestimated by a factor of 2 at both observation sites (Fig. 6 and Table S4). The high wind speed bias in winter (\sim factor of 2) should result in too rapid dispersion and could contribute to the negative bias, but the negative bias in the PBL heights should lead to higher predicted concentrations. Thus this negative bias is likely related to emissions (an indication of an underestimation of the heating fuel use).

The OC concentrations follow a similar seasonal cycle as BC and are also underpredicted (Fig. 6 and Table S4). Furthermore the OC/BC ratio is underpredicted by a factor of ~ 3 (Fig. 6). The observed OC/BC ratio follows a seasonal cycle, with values >15 in summer and ~ 5 in September through April. Part of this underprediction in OC and the OC/BC ratio is due to the fact that SOA is not estimated in the model. However a source contribution of OC using

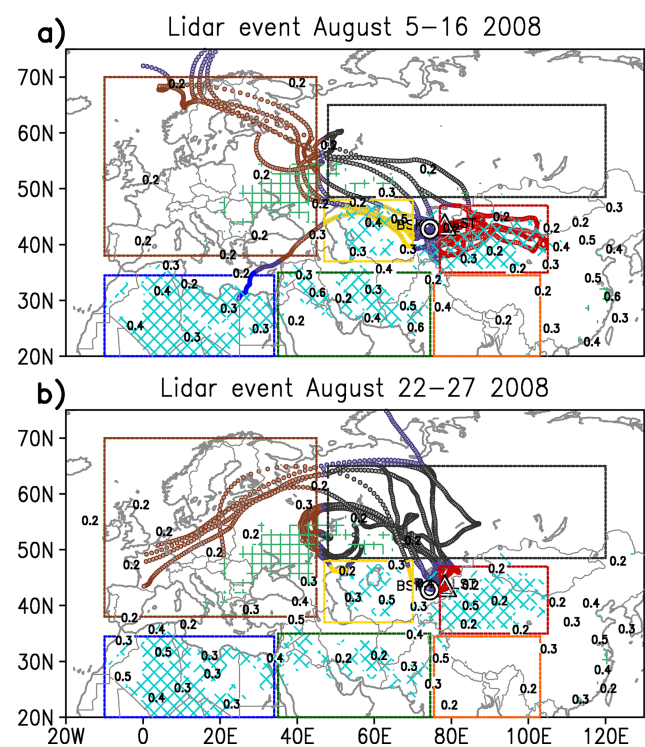


Figure 14. Ten-day air mass back trajectories for August 2008 (events 1 and 2 as denoted in Fig. 13) color-coded by source regions. The blue diamond and green square hatched areas denote the natural dust and biomass burning emission sources, while the numbers in black denote MODIS AOD contours averaged over the event time period and prior 10 days. The trajectories are color-coded by source regions: Africa (blue), Middle East (green), Central Asia (yellow), North Asian biomass ($>50^{\circ}$ N, black), Europe (brown), China (red), and South Asia (orange). “Lidar” denotes the LST site.

the filter data and chemical mass balance (CMB) approach found that SOA sources were very low in winter and only $\sim 20\%$ in summer (Miller-Schulze et al., 2011). Thus SOA cannot account for the model underprediction of winter values. There appears to be an underestimation of regional OC primary emissions. SOA can, however, help account for the large values of OC/BC observed in the summer and not predicted.

Biomass burning emissions cannot account for the underestimation in winter BC and OC. The largest impact of fires at the observation sites is in the late summer, when the fires are concentrated in western Russia and the wind direction is such that the smoke is transported into CA. Fires from South Asia can impact the sites associated with the fires and high pollution levels in northern India and with winds from the south, which can occur in late fall, but not frequently.

The fact that BC and OC are systematically underpredicted in the winter suggests that local/regional emissions during the heating season may be underestimated. This is supported by the results of the CMB analysis of OC discussed above that found the contribution from biofuel com-

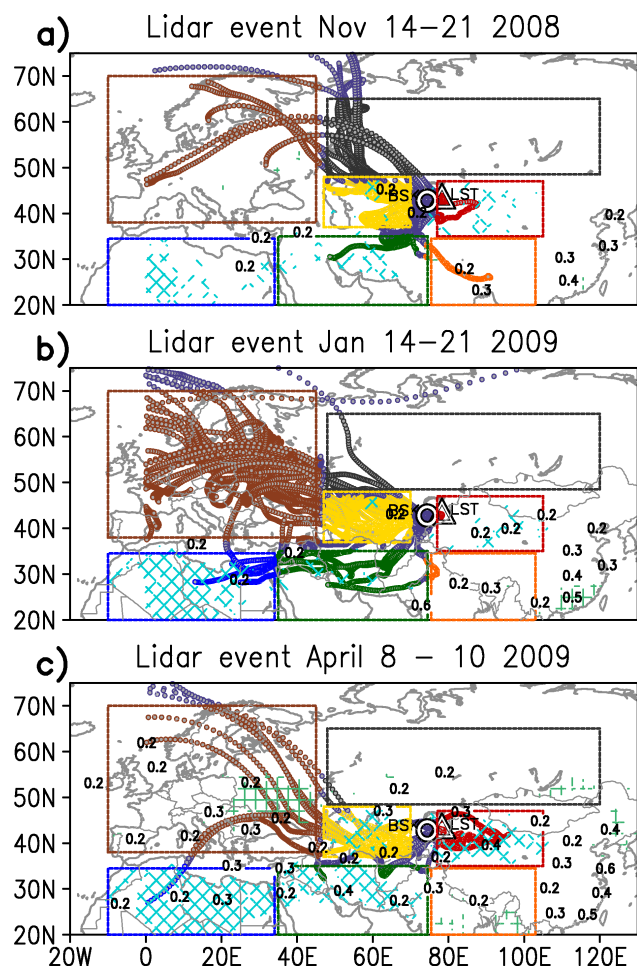


Figure 15. Same as Fig. 14 but for November 2008, January 2009, and April 2009 (events 3, 4, and 5 denoted in Fig. 13).

bustion increased 2–3 times in the fall and winter periods. The uncertainty in emissions can also be partly caused by the lack of seasonal emissions over this region as described earlier in Sect. 2.

3.7 Vertical distributions

Figure 13 shows the predicted weekly averaged vertical distributions of PM_{2.5}, dust, and BC for the entire simulation period at the LST site. These plots show more clearly that much of the variability in the PM loadings is associated with dust and biomass burning episodes (as represented by the enhancements in BC). Typically the high PM episodes show elevated PM mass that extends from the surface to 2 to 4 km. The vertical extents show a seasonality associated with seasonal variations in the PBL heights. These vertical distributions indicate that much of the transport of aerosols in CA occurs via low-altitude pathways. In some cases there are large amounts of dust and biomass burning aerosol in the 3–6 km altitude range that are decoupled from the surface

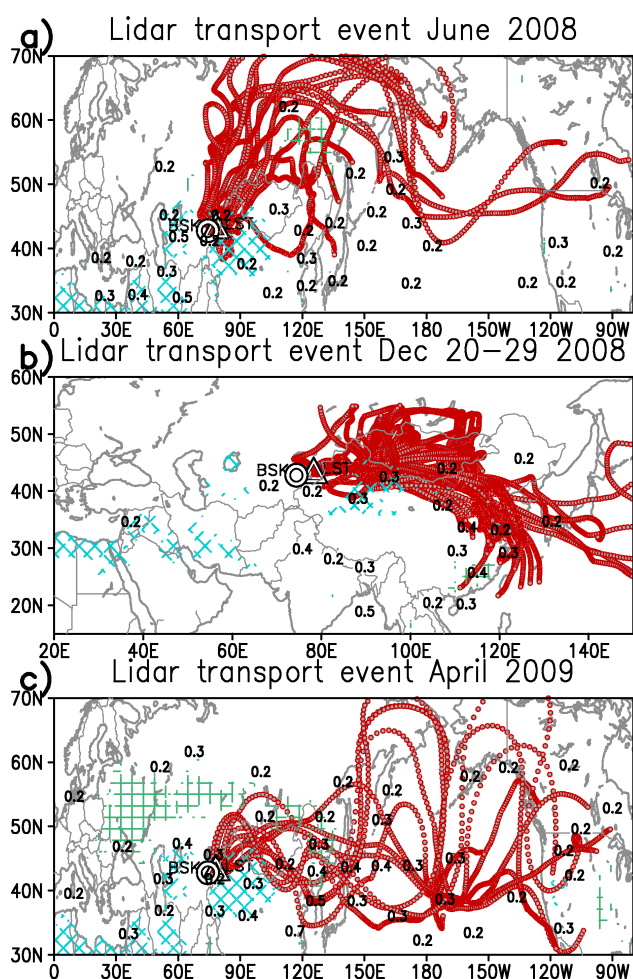


Figure 16. Ten-day air mass forward trajectories illustrating the seasonality in transport pathways out of CA for (a) June 2008, (b) December 2008, and (c) April 2009. The blue diamond and green square hatched areas denote the natural dust and biomass burning emission sources, respectively, while the numbers in black denote MODIS AOD contours averaged over the event time period and subsequent 10-day time window. “Lidar” denotes the LST site.

(e.g., dust in early May 2009), reflecting that some aerosols are lifted out of the boundary layer and are transported at high altitude over CA, enhancing AOD but not contributing to ground-level mass concentrations at the observation sites. These vertical features are confirmed by the aerosol extinction profiles observed at the LST site as discussed in Chen et al. (2012 b). The variation in weekly averaged AOD can be significant (Fig. 13 bottom panel) and is driven by variations in dust and biomass burning emissions.

3.8 Transport pathways

The three-dimensional 10-day air mass trajectories (described in Sect. 2.2) were utilized to further understand the transport pathways of air masses entering into and exiting out

of the CA region and its subsequent impact of source regions on the aerosol distributions at the CA sites.

3.8.1 Transport into CA

The air mass transport into CA is discussed through back trajectories associated with the five events labeled in Fig. 13. These five events represent transport episodes with elevated surface PM_{2.5} (averaged over the 3 h time window consistent with trajectory time step) with varying contributions from biomass burning, anthropogenic pollution, and dust sources. In each trajectory figure (Figs. 14 and 15), the regions with active dust (blue diamond hatching) and biomass burning emissions (green square hatching) for the event time period and prior 10 days are identified and MODIS AOD (values printed in black) overlaid. The trajectories are color-coded by region to distinguish the source impacts. The regions include Africa (blue), the Middle East (green), CA (yellow), North Asian biomass (> 50° N, black), Europe (brown), China (red), and South Asia (orange).

Figure 14 shows the first two events for August 2008. The first event in early August (Fig. 13, event labeled 1) is a high-dust event associated with trajectories from the west passing over the dust regions of the Aral Sea (~45° N, 55° E) and eastern trajectories passing over the Taklimakan region of western China (90–100° E, 40° N). These were both regions with active dust emissions as indicated by the elevated MODIS AOD values. Thus the PM increases during this event were due largely to dust emitted from deserts of CA and western China. The second event in the latter half of August is characterized by high levels of BC without dust. During this episode the transport to the site was under the influence of a high-pressure system located to the northwest and air masses were transported over the active fire region in western Russia.

Figure 15 shows winter and spring events. The November episode (event 3) is a period with elevated BC and PM_{2.5} from pollution sources from South Asia (including some fires) and western China and low fire and dust emission activity. The January episode (event 4) is a period of elevated BC with air masses coming from Europe, indicating the influence of anthropogenic pollution coming from this industrialized region, and from CA sources. Dust emissions from CA and Africa were low during this period. The final illustrative episode is for April 2009 (event 5), a period with both elevated levels of dust from western China, CA, and Africa and BC from both fire and anthropogenic pollution from European, CA, and Russian sources.

These examples provide insights into the source region contributions to PM mass in CA as presented in Figs. 11 and 12). CA is an ideal location to observe a variety of source regions as it is at the crossroad of transport patterns with air masses impacted from dust, anthropogenic activity, and biomass burning from different geographical regions.

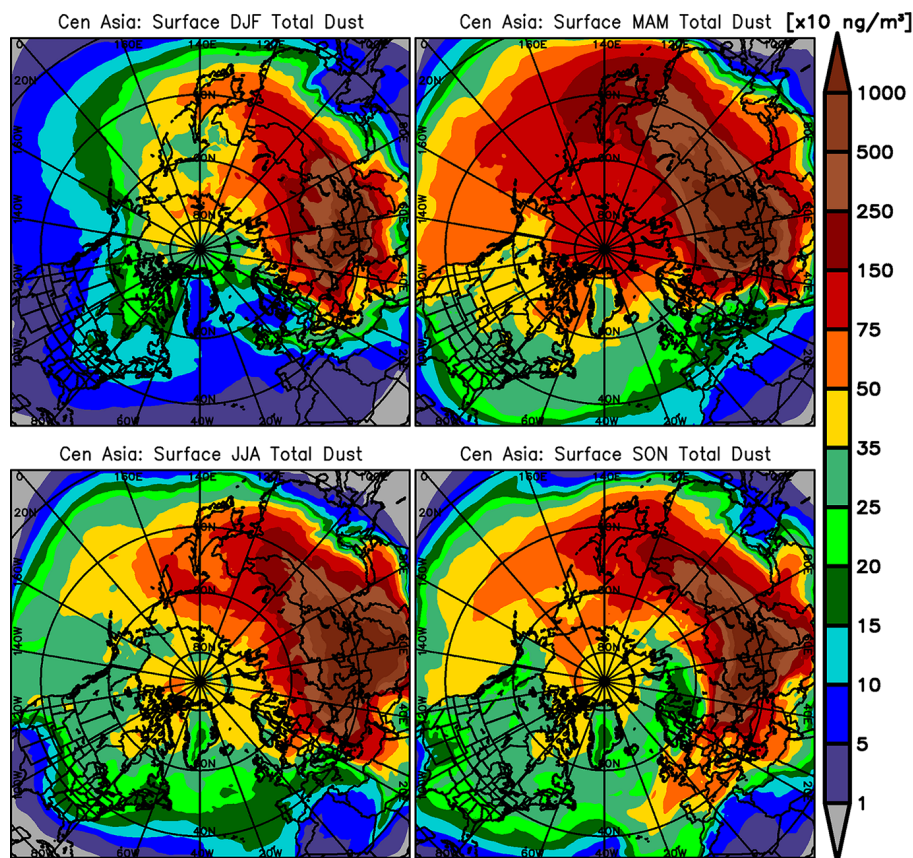


Figure 17. Seasonally averaged surface total dust (PM₁₀) concentrations from Central Asian dust emissions. DJF (top left panel) denotes the average for the months of December, January, and February. MAM (top right panel) denotes the average for months of March, April, and May. JJA (bottom left panel) denotes the average for months of June, July, and August. SON (bottom right panel) denotes average for months of September, October, and November.

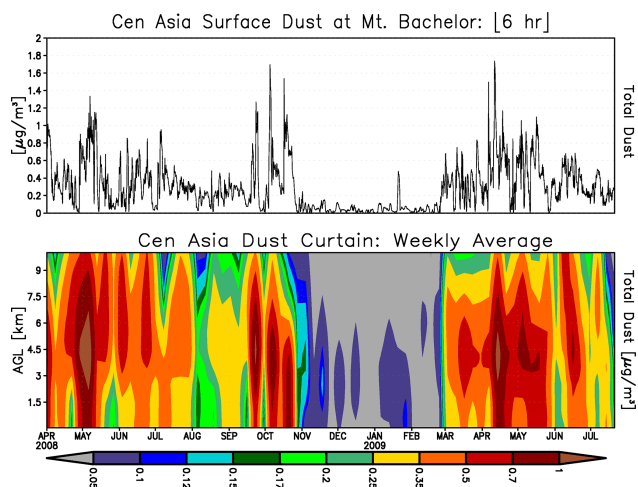


Figure 18. Time series of predicted surface concentration at 6 h time step (top panel) and weekly averaged time–altitude cross sections (bottom panel) of total dust (PM₁₀) from Central Asia dust emissions at Mt. Bachelor, Oregon, USA.

3.8.2 Long-range transport of CA sources

The transport pathways out of CA were also evaluated by calculating forward trajectories from the observation sites. Selected forward trajectories initialized at or below 1 km are used to represent the transport of boundary layer PM from CA and these are shown for summer, winter, and spring periods in Fig. 16. In these plots the MODIS AOD, dust, and fire emissions plotted for each event represent values averaged over the subsequent 10 days and trajectories were stopped if they impacted the surface. During the summer, outflow from CA is towards the north in association with the summer monsoon system. Figure 16a shows the subset of forward trajectories that reside for at least 3 days over the region 48–65° N during June 2008. Trajectories typically pass over Russia and reach into the Arctic and can also be caught in westerly storm tracks and reach the higher latitudes of the Northern Hemisphere. During the winter, air mass transport out of CA is associated with the winter monsoon system, and the transport pathway is over Mongolia and then over eastern China as seen in Fig. 16b. In this figure, forward trajectories that

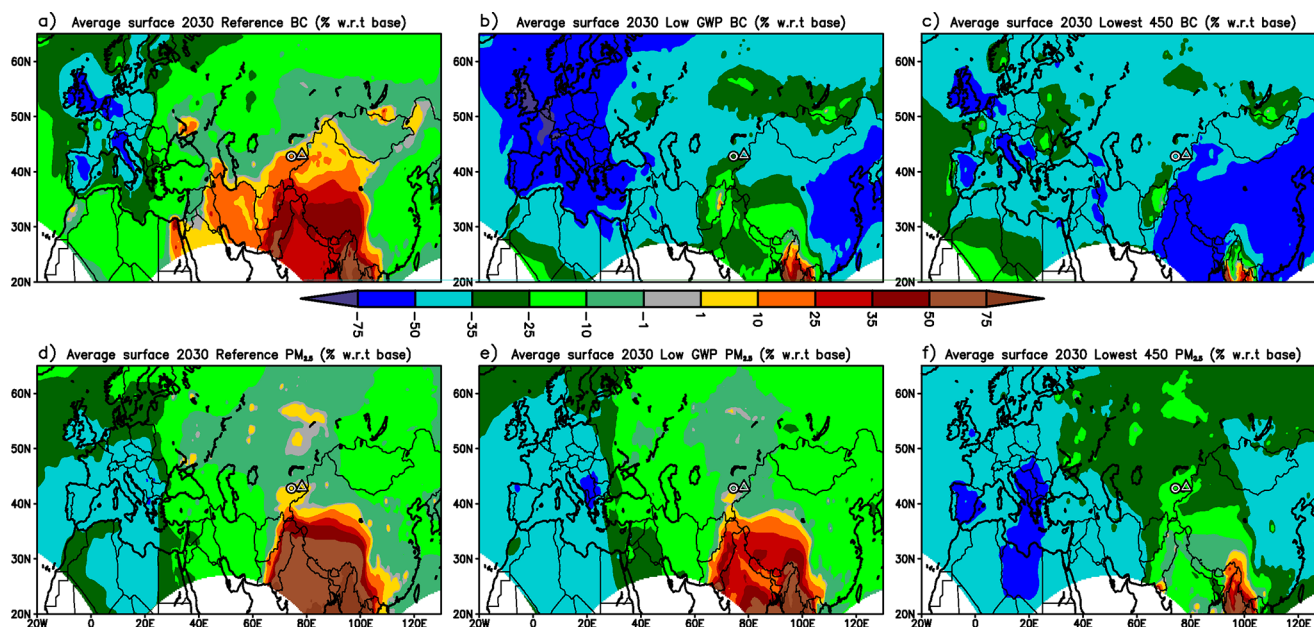


Figure 19. Percent change in simulated period mean surface BC and PM_{2.5} concentrations for future 2030 emission scenarios relative to the base year (2005), (a, d) reference 2030, (a, e) BC measures (low), and (c, f) BC (lowest) and greenhouse gas measures aimed at keeping CO₂ levels below 450 ppm. Refer to Sect. 2.3 for more details on emission scenarios.

pass over the region west of 130° E during late December 2008 are shown. Figure 16c illustrates transpacific transport of CA air masses. Plotted are the forward trajectories that stay within the 30–50° N region for at least 3 days during the month of April 2009. During the spring, transport from CA is dominated by strong westerly flows and air masses are transported over China, Korea, and Japan and then across the Pacific, reaching North America in 7–10 days.

PM arising from dust and anthropogenic emissions from CA impacts the entire Northern Hemisphere as illustrated in the hemispheric maps of seasonal average surface dust concentrations due to CA emissions only (Fig. 17). The predominant westerly flows in all seasons in the Northern Hemisphere result in the bulk of the CA emissions being transported to the west. The contribution of CA sources to surface PM concentrations of 0.35 μg m⁻³ or greater covers large portions of the Northern Hemisphere, including the Arctic, all of Asia, much of Europe, and portions of the continental USA.

There are episodic and seasonal components to the intercontinental transport as shown in the time series of the vertical profiles of PM_{2.5} at Mt. Bachelor, Oregon, USA (43.97° N, 121.69° W; 2700 m a.g.l.) (Fig. 18). The bulk of the CA particle transport takes place in the free troposphere and impacts surface concentrations in the USA as the boundary layer grows and entrains “plumes” aloft. This occurs most frequently in spring, summer, and fall. The episodic contributions of CA sources to surface concentrations can ex-

ceed 1.5 μg m⁻³. In the fall, there is also strong transport of dust from CA across Europe and out into the Atlantic.

3.9 Future scenarios

How might PM levels change in CA over the next few decades? To address this question, simulations were repeated for various emission scenarios developed and used in the WMO/UNEP assessment on short-lived climate pollutants (Shindell et al., 2012) as described in Sect. 2. Dust and biomass burning emissions and meteorology were the same as those used in the 2008/2009 simulations. The period mean changes in surface BC and PM_{2.5} concentrations in 2030 for the reference scenario are shown in Fig. 19a and d, respectively. This scenario reflects all present agreed policies affecting emissions and assumes that they are fully implemented. Under this scenario PM_{2.5} increases significantly in South Asia and western China (> 50 %) and in parts of CA, including the area where the sampling sites are located. PM_{2.5} decreases in western Europe and eastern China (< 10 %). BC surface concentrations show a similar pattern to PM_{2.5}, although covering larger portions of CA with relatively larger increases in BC than in PM_{2.5}. These results suggest that health impacts and climate warming due to BC and PM_{2.5} may increase in coming decades unless additional emission control measures are implemented.

Results for two other scenarios are also presented in Fig. 19. One scenario specifically targets BC emission reductions in recognition that BC is also a major contributor to atmospheric warming (Ramanathan and Carmichael, 2008).

Table 1. Summary of changes in Central Asia (CA) region (see Fig. 1 for CA region definition) emissions and concentration under the future emission scenarios (see Sect. 3.9 for more details).

Emission scenario	Emissions Gg yr ⁻¹			Emissions change (%) w.r.t to base 2005		
	BC	SO ₂	PM _{2.5}	BC	SO ₂	PM _{2.5}
Base 2005	39	1130	197			
Reference 2030	47	1326	224	22.1	17.3	13.9
Low GWP 2030	27	1325	177	-31.1	17.3	-10.1
Lowest GWP + 450	21	1058	115	-46.9	-6.4	-41.5
	Concentration (µg m ⁻³)			Concentration change (%) w.r.t to base 2005		
	BC	SO ₄	PM _{2.5}	BC	SO ₄	PM _{2.5}
Base 2005	0.17	3.04	4.26			
Reference 2030	0.16	2.65	4.03	-4.2	-12.6	-5.3
Low GWP 2030	0.11	2.64	3.85	-36.6	-13	-9.5
Lowest GWP + 450	0.10	2.04	3.06	-38.5	-32.9	-28

These additional measures significantly reduce 2030 BC concentrations by greater than 35 % throughout most of the domain, with only a few regions (e.g., Myanmar and eastern Afghanistan) showing increases in BC relative to 2005 levels. This scenario assumes that all BC emission reduction measures are perfectly implemented and 100 % effective. BC measures also impact emissions of co-emitted pollutants (e.g., OC and SO₂). PM_{2.5} concentrations under this scenario (Fig. 19e) are reduced, but by much smaller amounts, and concentrations still increase relative to 2005 over large regions of South Asia and western China, and parts of CA. These results suggest that health impacts in these regions may increase due to the PM_{2.5} increases, whereas positive radiative forcing and health effects due to BC may decrease. When the BC measures are used along with greenhouse gas measures aimed at keeping CO₂ levels below 450 ppm, the PM_{2.5} levels in South Asia are lower than 2005 levels (Fig. 19f), with a few exceptions (one being the Myanmar region). This is due to the large decreases in SO₂ and NO_x emissions under this scenario, resulting in significant reductions in particulate nitrate and sulfate (e.g., a ~ 30 % increase in particulate sulfate in CA).

To get a regional perspective of how the future emission changes would specifically impact the CA region (see Fig. 1 for the CA region definition used in this study), we have summarized the changes in emissions and the corresponding concentrations in Table 1. The reference 2030 emissions scenario reports an increase in emissions of BC, SO₂ and PM_{2.5} over Central Asia by ~ 22, 17, and 14 %, respectively, with regard to base 2005 levels. However, the corresponding BC, SO₄, and anthropogenic portions of PM_{2.5} decrease by ~ 5, 12, and 5 %, respectively. This suggests that on average the concentration levels decrease even though CA emissions increase due to long-range transport of pollutants into

the CA region from the surrounding regions but locations within CA still increase when dominated by local sources. The low-GWP emission scenario predicts decreases in BC and PM_{2.5} emissions by 31 and 10 %, respectively, with the corresponding decrease in concentrations by ~ 37 and 10 %, respectively, while SO₂ emissions remained the same as the reference 2030 scenario. The lowest + 450 ppm scenario shows a consistent decreasing trend in emissions and concentration of all the species. This analysis suggests that the impact of the changes in major source region emissions and their subsequent transport to Central Asia will play a major role in determining the future aerosol levels in CA.

4 Summary

AOD in CA during the period April 2008 through July 2009 averaged ~ 0.3 and displayed a seasonal cycle, with the lowest values in the winter and highest values in spring to mid-summer with observed values of AOD > 0.6 and even > 0.8. Surface PM_{2.5} measured at two sites in eastern CA averaged ~ 10 µg m⁻³ but with large variability (hourly values from 2 to 90 µg m⁻³). Surface concentrations of PM also showed a seasonal cycle with peak values and largest variability in the spring/summer, and lowest values and variability in the winter. BC at these sites averaged ~ 0.1 µg m⁻³, with peak values (~ 1 µg m⁻³) in the winter.

The seasonal cycles and source sector and source region contributions to PM in CA were analyzed using the STEM chemical transport model. Dust was the largest component of the PM_{2.5} and PM₁₀ mass in the region in all seasons except winter, whereas sulfate was the largest anthropogenic component of the PM_{2.5} mass. Dust was also found to be the major driver of the seasonal cycles of AOD and PM concen-

trations. On an annual basis the power and industrial sectors were the most important contributors to PM_{2.5}, while residential and transportation were the most important sectors for BC. Open biomass burning within and outside the region also contributed to elevated PM and BC concentrations and to the temporal variability.

The model simulations showed a systematic overprediction of PM mass. This is most likely due in large part to the overprediction in dust. Carbonaceous PM was underpredicted, and it is speculated that the winter emissions associated with residential heating may be underestimated in the current emissions inventory. The predicted wind speeds were biased high (by ~30%) and the direction had a southwest bias. The high bias in wind speeds may also contribute to the overprediction in PM₁₀, as dust emissions depend strongly on wind speed. Efforts to improve the dust emissions and to improve the wind speed and direction predictions using a finer model resolution are planned. Additional efforts are needed to improve the anthropogenic emissions estimates for CA.

Currently there are few measurements in CA that can be used to quantify the intercontinental transport of pollution from Europe to Asia. The analysis of the transport pathways and variations in PM mass and composition observed at the two sites in CA demonstrate that this region is strategically located to characterize regional and intercontinental transport of pollutants. Aerosols at these sites were shown to reflect dust, biomass burning, and anthropogenic sources from South, East, and Central Asia; Europe; and Russia depending on the time of year. For example, during the spring fine particles from Europe and Africa were transported to CA, on to eastern Asia, and then across the Pacific to North America.

Observations of PM and its composition in this region are of growing importance as it is estimated that PM_{2.5} levels are likely to increase significantly in Central and South Asia and western China over the next few decades. Simulations for a reference 2030 emission scenario showed that BC concentrations had a larger relative increase than PM_{2.5} concentrations. This suggests that health impacts and climate warming associated with these pollutants may increase over the next decades unless additional control measures are implemented. Continued pollutant observations in CA will help to characterize the changes that are rapidly taking place in the region.

The Supplement related to this article is available online at doi:10.5194/acp-15-1683-2015-supplement.

Acknowledgements. The US Environmental Protection Agency through its Office of Research and Development funded this study and collaborated in the research described here as a component of the International Science & Technology Center (ISTC) project no. 3715 (Transcontinental Transport of Air Pollution

from Central Asia to the US). The University of Iowa activities were also supported in part by the following grants: EPA (RD-83503701-0), NASA (NNX08AH56G), NSF (1049140), NCRR (UL1RR024979), and Fulbright-CONICYT (15093810). The contents of this study are solely the responsibility of the authors and do not necessarily represent the official views of the funding institutions. This manuscript has been subjected to US EPA review and approved for publication. We thank all the PIs and their staff for establishing and maintaining the AERONET sites that have been used in this study. We would also like to acknowledge the Network Center for EANET and the EMEP Chemical Coordinating Centre for the PM₁₀ measurements used in this study.

Edited by: J. West

References

- Adhikary, B., Carmichael, G. R., Tang, Y., Leung, L. R., Qian, Y., Schauer, J. J., Stone, E. a., Ramanathan, V. and Ramana, M. V.: Characterization of the seasonal cycle of south Asian aerosols: A regional-scale modeling analysis, *J. Geophys. Res.*, 112, D22S22, doi:10.1029/2006JD008143, 2007.
- Anenberg, S. C., Schwartz, J., Shindell, D., Amann, M., Faluvegi, G., Klimont, Z., Maenhout, G., Pozzoli, L., van Dingenen, R., Vignati, E., Emberson, L., Muller, N. Z., West, J. J., Williams, M., Demkine, V., Hicks, W. K., Kuylensstierna, J., Raes, F., and Ramanathan, V.: Global air quality and health co-benefits of mitigating near-term climate change through methane and black carbon emission controls, *Environ. Health Perspect.*, 120, 831–839, 2012.
- Bates, T. S., Anderson, T. L., Baynard, T., Bond, T., Boucher, O., Carmichael, G., Clarke, A., Erlick, C., Guo, H., Horowitz, L., Howell, S., Kulkarni, S., Maring, H., McComiskey, A., Middlebrook, A., Noone, K., O'Dowd, C. D., Ogren, J., Penner, J., Quinn, P. K., Ravishankara, A. R., Savoie, D. L., Schwartz, S. E., Shinozuka, Y., Tang, Y., Weber, R. J., and Wu, Y.: Aerosol direct radiative effects over the northwest Atlantic, northwest Pacific, and North Indian Oceans: estimates based on in-situ chemical and optical measurements and chemical transport modeling, *Atmos. Chem. Phys.*, 6, 1657–1732, doi:10.5194/acp-6-1657-2006, 2006.
- Bauer, S. E., Koch, D., Unger, N., Metzger, S. M., Shindell, D. T., and Streets, D. G.: Nitrate aerosols today and in 2030: a global simulation including aerosols and tropospheric ozone, *Atmos. Chem. Phys.*, 7, 5043–5059, doi:10.5194/acp-7-5043-2007, 2007.
- Carmichael, G. R., Adhikary, B., Kulkarni, S., D'Allura, A., Tang, Y., Streets, D., Zhang, Q., Bond, T. C., Ramanathan, V., Jamroensan, A., and Marrapu, P.: Asian aerosols: current and year 2030 distributions and implications to human health and regional climate change, *Environ. Sci. Technol.*, 43, 5811–5817, 2009.
- Chen, B., Sverdluk, L. G., Imashev, S. A., Solomon, P. A., Lantz, J., Schauer, J. J., Shafer, M. M., Artamonova, M. S., and Carmichael, G.: Empirical relationship between particulate matter and aerosol optical depth over Northern Tien-Shan, Central Asia, *Air Quality, Atmosphere & Health*, 6.2, 358–396, doi:10.1007/s11869-012-0192-5, 2012.

- Chen, B. B., Imashev, S. A., Sverdlik, L. G., Solomon, P. A., Lantz, J., Schauer, J. J., Shafer, M. M., Artamonova, M. S. and Carmichael, G. R.: Ozone Variations over Central Tien-Shan in Central Asia and Implications for Regional Emissions Reduction Strategies, *Aerosol. Air. Qual. Res.*, 13, 555–562 doi:10.4209/aaqr.2012.06.0156, 2013.
- Chung, C. E., Ramanathan, V., Carmichael, G., Kulkarni, S., Tang, Y., Adhikary, B., Leung, L. R., and Qian, Y.: Anthropogenic aerosol radiative forcing in Asia derived from regional models with atmospheric and aerosol data assimilation, *Atmos. Chem. Phys.*, 10, 6007–6024, doi:10.5194/acp-10-6007-2010, 2010.
- D'Allura, A., Kulkarni, S., Carmichael, G. R., Finardi, S., Adhikary, B., Wei, C., Streets, D., Zhang, Q., Pierce, R. B., Al-Saadi, J. A., Diskin, G., Wennberg, P.: Meteorological and air quality forecasting using the WRF–STEM model during the 2008 ARCTAS field campaign, *Atmos. Environ.*, 45, 6901–6910, doi:10.1016/j.atmosenv.2011.02.073, 2011.
- Denier van der Gon, H., Visschedijk, A., Droge, R., Mulder, M., Johansson, C., and Klimont, Z.: A high resolution emission inventory of particulate elemental carbon and organic carbon for Europe in 2005, 7th International Conference on Air Quality – Science and Application (Air Quality 2009), Istanbul, 2009.
- Emerson, J. W., Hsu, A., Levy, M. A., de Sherbinin, A., Mara, V., Esty, D. C., and Jaiteh, M.: Environmental Performance Index and Pilot Trend Environmental Performance Index, Yale Center for Environmental Law and Policy, New Haven, 2012.
- Freitas, S. R., Longo, K. M., Chatfield, R., Latham, D., Silva Dias, M. A. F., Andreae, M. O., Prins, E., Santos, J. C., Gielow, R., and Carvalho Jr., J. A.: Including the sub-grid scale plume rise of vegetation fires in low resolution atmospheric transport models, *Atmos. Chem. Phys.*, 7, 3385–3398, doi:10.5194/acp-7-3385-2007, 2007.
- Freitas, S. R., Longo, K. M., Trentmann, J., and Latham, D.: Technical Note: Sensitivity of 1-D smoke plume rise models to the inclusion of environmental wind drag, *Atmos. Chem. Phys.*, 10, 585–594, doi:10.5194/acp-10-585-2010, 2010.
- Ginoux, P., Chin, M., Tegen, I., Prospero, J. M., Holben, B., Dubovik, O. and Lin, S.-J.: Sources and distributions of dust aerosols simulated with the GOCART model, *J. Geophys. Res.-Atmos.*, 106, 20255–20273, doi:10.1029/2000JD000053, 2001.
- Gong, S. L.: A parameterization of sea-salt aerosol source function for sub- and super-micron particles, *Global Biogeochem. Cy.*, 17, 1097, doi:10.1029/2003GB002079, 2003.
- Grell, G. A., Peckham, S. E., Schmitz, R., McKeen, S. A., Frost, G., Skamarock, W. C., and Eder, B.: Fully coupled “online” chemistry within the WRF model, *Atmos. Environ.* 39, 6957–6975, 2005.
- Grell, G., Freitas, S. R., Stuefer, M., and Fast, J.: Inclusion of biomass burning in WRF-Chem: impact of wildfires on weather forecasts, *Atmos. Chem. Phys.*, 11, 5289–5303, doi:10.5194/acp-11-5289-2011, 2011.
- Guttikunda, S., Tang, Y., Carmichael, G., Kurata, G., Pan, L., Streets, D., Woo, J.-H., Thongboonchoo, N., and Fried, A.: Impacts of Asian megacity emissions on regional air quality during spring 2001, *J. Geophys. Res.*, 110, D20301, doi:10.1029/2004JD004921, 2005.
- Hsu, N. C., Tsay, S.-C., King, M. D., and Herman, J. R.: Aerosol properties over bright-reflecting source regions, *IEEE T. Geosci. Remote.*, 42, 557–569, doi:10.1109/TGRS.2004.824067, 2004.
- Hsu, N. C., Tsay, S.-C., King, M. D., and Herman, J. R.: Deep Blue Retrievals of Asian Aerosol Properties During ACE-Asia, *IEEE T. Geosci. Remote.*, 44, 3180–3195, doi:10.1109/TGRS.2006.879540, 2006.
- HTAP: Hemispheric Transport of Air Pollution 2010 (Executive Summary), available at: http://www.htap.org/publications/2010_report/2010_Final_Report/EBMeeting2010.pdf (last access: 26 February 2013), 2010.
- Huang, M., G. Carmichael, S. Kulkarni, D. Streets, Z. Lu, Q. Zhang, B. Pierce, Y. Kondo, J. Jimenez-Palacios, M. J. Cubison, B. E. Anderson, and A. Wisthaler: Sectoral and geographical contributions to summertime continental United States (CONUS) black carbon spatial distributions, *Atmos. Environ.*, 51, 165–174, doi:10.1016/j.atmosenv.2012.01.021, 2012.
- Hubanks, P. A., King, M. A., Platnick, S., and Pincus, R.: MODIS atmosphere L3 gridded product algorithm theoretical basis document, MODIS Algorithm Theoretical Basis Document No. ATBD-MOD-30, available at: http://modis-atmos.gsfc.nasa.gov/_docs/L3_ATBD_2008_12_04.pdf, 2008.
- Kurata, G., Carmichael, G. R., Streets, D. G., Kitada, T., Tang, Y., Woo, J. H., and Thongboonchoo, N.: Relationships between emission sources and air mass characteristics in East Asia during the TRACE-P period, *Atmos. Environ.*, 38, 6977–6987, 2004.
- Levy, R. C., Remer, L. A., Mattoo, S., Vermote, E. F., and Kaufman, Y. J.: Second-generation operational algorithm: Retrieval of aerosol properties over land from inversion of Moderate Resolution Imaging Spectroradiometer spectral reflectance, *J. Geophys. Res.-Atmos.*, 112, D13211, doi:10.1029/2006JD007811, 2007.
- Lu, Z., Zhang, Q., and Streets, D. G.: Sulfur dioxide and primary carbonaceous aerosol emissions in China and India, 1996–2010, *Atmos. Chem. Phys.*, 11, 9839–9864, doi:10.5194/acp-11-9839-2011, 2011.
- Miller-Schulze, J. P., Shafer, M. M., Schauer, J. J., Solomon, P. a., Lantz, J., Artamonova, M., Chen, B., Imashev, S., Sverdlik, L., Carmichael, G. R. and Deminter, J. T.: Characteristics of fine particle carbonaceous aerosol at two remote sites in Central Asia, *Atmos. Environ.*, 45, 6955–6964, doi:10.1016/j.atmosenv.2011.09.026, 2011.
- Ramanathan, V. and Carmichael, G.: Global and regional climate changes due to black carbon, *Nat. Geosci.*, 1, 221–227, available at: <http://www.nature.com/nggeo/journal/vaop/ncurrent/full/ngeo156.html> (last access: 18 February 2013), 2008.
- Remer, L. A., Kaufman, Y. J., Tanré, D., Mattoo, S., Chu, D. A., Martins, J. V. Li, R.-R., Ichoku, C., Levy, R. C., Kleidman, R. G., Eck, T. F., Vermote, E., and Holben, B.N.: The MODIS aerosol algorithm products and validation, *J. Atmos. Sci.*, 62, 947–973, doi:10.1175/JAS3385.1, 2005.
- Shindell, D., Kuylenstierna, J. C. I., Vignati, E., van Dingenen, R., Amann, M., Klimont, Z., Anenberg, S. C., Muller, N., Janssens-Maenhout, G., Raes, F., Schwartz, J., Faluvegi, G., Pozzoli, L., Kupiainen, K., Hoglund-Isaksson, L., Emberson, L., Streets, D., Ramanathan, V., Hicks, K., Kim Oanh, N. T., Milly, G., Williams, M., Demkine, V., and Fowler, D.: Simultaneously mitigating near-term climate change and improving human health and food security, *Science*, 335, 183–189, doi:10.1126/science.1210026, 2012.
- Skamarock, W. C., Klemp, J. B., Dudhia, J., Gill, D. O., Barker, D. M., Duda, M. G., Huang, X.-Y., Wang, W., and Powers, J. G.: A Description of the Advanced Research WRF, Ver-

- sion 3, Technical Report NCAR/TN475+STR, National Center for Atmospheric Research Technical Note, Boulder, Colorado, 2008.
- UNEP: Framework Convention on Environmental Protection for Sustainable Development in Central Asia, Regional Resource Centre for Asia and the Pacific (PRC.AP), available at: <http://www.rrcap.ait.asia/library/ca-report/Brief-Convention.doc> (last access: 25 April 2014), 2006.
- UNEP and WMO: Integrated Assessment of Black Carbon and Tropospheric Ozone: Summary for Decision Makers, available at: http://www.unep.org/dewa/Portals/67/pdf/BlackCarbon_SDM.pdf (last access: 26 February 2013), 2011.
- Uno, I., Satake, S., Carmichael, G. R., Tang, Y., Wang, Z., Takemura, T., Sugimoto, N., Shimizu, A., Murayama, T., Cahill, T. A., Cliff, S., Uematsu, M., Ohta, S., Quinn, P. K., and Bates, T. S.: Numerical study of Asian dust transport during the spring-time of 2001 simulated with the Chemical Weather Forecasting System (CFORS) model, *J. Geophys. Res.*, 109, D19S24, doi:10.1029/2003JD004222, 2004.
- Visschedijk, A., Denier van der Gon, H., Droge, R., and van der Brugh, H.: A European high resolution and size-differentiated emission inventory for elemental and organic carbon for the year 2005, TNO-034-UT-2009-00688_RPT-ML, TNO, Utrecht, 2009.
- Wang, W., Bruyere, C., Duda, M., Dudhia, J., Gill, D., Lin, H.-C., Michalakes, J., Rizvi, S., and Zhang, X.: Version 3 Modeling System User's Guide January 2011, National Center for Atmospheric Research (NCAR), available at: http://www.mmm.ucar.edu/wrf/users/docs/user_guide_V3.2/ARWUsersGuideV3.pdf (last access: 25 April 2014), 2011.
- Wesely, M. L. and Hicks, B. B.: A review of the current status of knowledge on dry deposition, *Atmos. Environ.*, 34, 2261–2282, doi:10.1016/S1352-2310(99)00467-7, 2000.
- Whish-Wilson, P.: The Aral Sea environmental health crisis the desiccation of the Aral Sea health in the Aral Sea region, *Journal of Rural and Remote Environmental Health*, 1, 29–34, available at: <http://www.jcu.edu.au/jrtph/vol/v01whish.pdf> (last access: 25 April 2014), 2002.
- Wiedinmyer, C., Akagi, S. K., Yokelson, R. J., Emmons, L. K., Al-Saadi, J. A., Orlando, J. J., and Soja, A. J.: The Fire INventory from NCAR (FINN): a high resolution global model to estimate the emissions from open burning, *Geosci. Model Dev.*, 4, 625–641, doi:10.5194/gmd-4-625-2011, 2011.
- Zhang, Q., Streets, D. G., Carmichael, G. R., He, K. B., Huo, H., Kannari, A., Klimont, Z., Park, I. S., Reddy, S., Fu, J. S., Chen, D., Duan, L., Lei, Y., Wang, L. T., and Yao, Z. L.: Asian emissions in 2006 for the NASA INTEX-B mission, *Atmos. Chem. Phys.*, 9, 5131–5153, doi:10.5194/acp-9-5131-2009, 2009.